university of groningen

Bachelor Thesis

Production of ^{41}Ar by thermal neutron capture in proton therapy

Author:
Fleur Vialle
S3687570

First Supervisor:
Peter Dendooven
Second Supervisor:
Sytze Brandenburg

Department of Radiation Oncology
University Medical Centre Groningen
University of Groningen
July 2, 2021

Abstract

In this research the amount of ^{41}Ar produced by thermal neutron activation at the Groningen Proton Therapy Center (GPTC) was investigated. An indirect measurement technique was used, where Na atoms in $NaHCO_3$ targets were neutron-activated instead of pure argon. The incident effective neutron flux was determined from the irradiated $NaHCO_3$ samples and combined with the neutron capture cross-section of ^{40}Ar to obtain an estimate for the produced ^{41}Ar activity. Initially, this indirect measurement technique was studied using an Am-Be neutron source at the Particle Therapy Research Center (PARTREC). It was determined that $NaHCO_3$ is a better sodium-containing substance for measuring the incident neutron flux than NaCl because of the significant thermal neutron absorption by chlorine in NaCl. Moreover, the effective neutron flux incident on an $NaHCO_3$ sample was compared with the effective neutron flux seen by neutron-activated argon. These were found to be approximately equal. Therefore, the flux determined using the Na activation method can be used for calculating the ^{41}Ar production. Finally, eight $NaHCO_3$ samples were placed throughout the cyclotron bunker and treatment room of the GPTC for an entire day of patient irradiations. The effective neutron flux incident on each sample was calculated and used to estimate the produced ^{41}Ar activity concentration. The activity in the treatment room and near the entrance maze of the bunker were found to be smaller than 0.3 Bqm^{-3}. The produced ^{41}Ar activity concentrations in the bunker ranged from $0.007(2) \times 10^3$ Bqm^{-3} near the exit maze up to $23(8) \times 10^3$ Bqm^{-3} close to the energy degrader. The total ^{41}Ar activity discharged from the cyclotron bunker into the atmosphere was found to be 3 GBq, which is well below the licensed discharge limit of 8 GBq per year.

Acknowledgements

I would like to thank Sytze Brandenburg, Peter Dendooven, Marc-Jan van Goethem and Emiel van der Graaf for their help, guidance and support during this project.

Contents

1 Introduction

During proton therapy a beam of protons is accelerated with the use of a particle accelerator. Secondary neutrons are produced when these high-energy protons interact with the patient or accelerator components like filters and beam collimators. Part of these high-energy neutrons thermalize through interactions with for example the concrete walls. These thermal neutrons will induce radioactivity in surrounding materials or lead to the activation of air via neutron capture reactions. One of the radioactive isotopes generated through thermal neutron activation is ^{41}Ar. It is produced from ^{40}Ar, which makes up 0.93% of the air around us[1]. Radioactive ^{41}Ar decays to the stable isotope ^{41}K via β-decay resulting in the emission of gamma rays. This radioactive decay occurs with a half-life of 110 minutes.[2] Since the half-life is quite long, the radioactive argon produced during proton therapy can leave the building through the ventilation system. This results in extra radioactivity in the atmosphere contributing to radiation exposure of the general public. [3, 4]

The aim of this research is to estimate the amount of ^{41}Ar produced by thermal neutron capture in proton therapy. For this purpose experiments were performed both at the accelerator facility at the Particle Therapy Research Center (PARTREC) of the UMCG [5](formerly part of the KVI-Center for Advanced Radiation Technology KVI-CART) and at the UMCG Groningen Proton Therapy Center (GPTC).

The production of ^{41}Ar at the proton center could be measured directly by activating pure argon in a gas bottle. However, since the argon will be activated over the course of a full day of patient irradiations, which lasts approximately 15 hours, and the half-life of ^{41}Ar is only 110 minutes, the ^{41}Ar activity produced during the first patient irradiations will already be lost once the gamma-ray spectrum is measured at the end of the treatment day. Therefore, the production of ^{41}Ar is measured indirectly by activating sodium. An equivalent neutron capture reaction, as in the production of ^{41}Ar, produces the radioactive isotope ^{24}Na from ^{23}Na. ^{24}Na has a relatively long half-life of almost 15 hours [2]. Neutron activation at the proton center for an entire patient treatment day is therefore not an issue. From the activation of sodium the thermal neutron flux can be determined. This neutron flux together with the thermal neutron capture cross-section of ^{40}Ar can then be used to calculate the amount of ^{41}Ar produced.

Before performing any measurements at the proton center, this indirect measurement technique is studied at the PARTREC facility. $NaHCO_3$ and NaCl samples, both containing sodium, are irradiated by an Am-Be neutron source. The determined neutron flux of an argon gas bottle irradiated by the same source is compared to the measured neutron fluxes of $NaHCO_3$ and NaCl to establish whether $NaHCO_3$ or NaCl can best be used for the indirect measurement of ^{41}Ar production at the GPTC.

2 Theory

Particle interactions with matter

Protons and neutrons are the main particles involved in neutron capture reactions induced in proton therapy. In the following sections the main interaction mechanisms of both protons and neutrons with matter are described. It is based on the books of Cember and Johnson[6], Turner[7], Knoll[8], Cottingham and Greenwood[9], Cherry et al.[10] and Ahmed[11]. Furthermore, articles by Newhauser and Zhang[12], Pérez-Andújar et al.[13] were used as a resource, along with an online source[14].

2.1 Proton interaction with matter

Protons can interact with an atom or nucleus in several ways. The main interaction mechanisms are: Coulomb interactions with either atomic electrons or atomic nuclei, Bremsstrahlung and nuclear interactions. Coulomb interactions and Bremsstrahlung result in energy loss of the proton, a change in trajectory of the incident proton or both. Nuclear interactions, however, result in the absorption of the primary proton by the nucleus and creation of secondary particles like neutrons and other spallation products. This latter type of interaction is important for the production of neutrons in beam-modifying devices such as energy degraders, collimators and scatterers used for proton beam therapy.

2.2 Neutrons

Classification

Neutrons can be classified into categories according to their energy. The first group of neutrons have energies above approximately 0.1 MeV. These neutrons are called fast neutrons.

At lower energies, neutrons are in thermal equilibrium with their surroundings. These so-called thermal neutrons follow the Maxwell-Boltzmann distribution for gas molecules. The Maxwell-Boltzmann distribution in terms of energy is given by[6]:

$$f(E) = \frac{2\pi}{(\pi k_B T)^{3/2}} e^{-E/k_B T} \sqrt{E} \tag{1}$$

where $f(E)$ is the fraction of gas molecules or neutrons with an energy between E and $E + dE$ (in J or eV), k_B is the Boltzmann constant (in J/K or eV/K) and T is the absolute temperature of the gas molecules or neutrons (in K).

According to the Maxwell-Boltzmann distribution, the most probable energy and mean energy as a function of temperature T are given by[8]:

$$E_{mp} = k_B T \tag{2}$$

$$E_{mean} = \frac{3}{2} k_B T \tag{3}$$

At room temperature (293 K) the most probable energy of thermal neutrons is thus 0.025 eV. The average energy of thermal neutrons at room temperature is equal to 0.038 eV.

For thermal neutrons in a gas, the mean free path λ_m (in cm), which is the average distance travelled between collisions, can be computed from[11]:

$$\lambda_m = \frac{1}{\sqrt{2}\sum_i n_i \sigma_{tot,i}} \tag{4}$$

where

n_i = atomic density corresponding to atoms of type i in the gas (cm^{-3})
$\sigma_{tot,i}$ = total cross-section corresponding to atom of type i (cm^2)

Neutrons with energies between those for thermal and fast neutrons are called slow, intermediate or resonance neutrons.

Neutron interaction with matter

When a neutron encounters a nucleus, there exist several interaction mechanisms. These different types of neutron interactions are illustrated in Figure 1. Scattering is one of these interactions and can take place in two ways, namely inelastically and elastically. The scattering is elastic when the total kinetic energy of the nucleus and the neutron is conserved in the collision. When neutrons undergo inelastic scattering, the total kinetic energy is not conserved. Instead, part of the kinetic energy is converted into excitation energy of the nucleus.

Another type of interaction is absorption or neutron capture. As the name suggests, the neutron is captured by the nucleus, after which the nucleus is in an excited state. The nucleus de-excites by emission of charged particles like alpha particles or protons, neutrons or by the emission of gamma rays. The latter is called radiative capture.

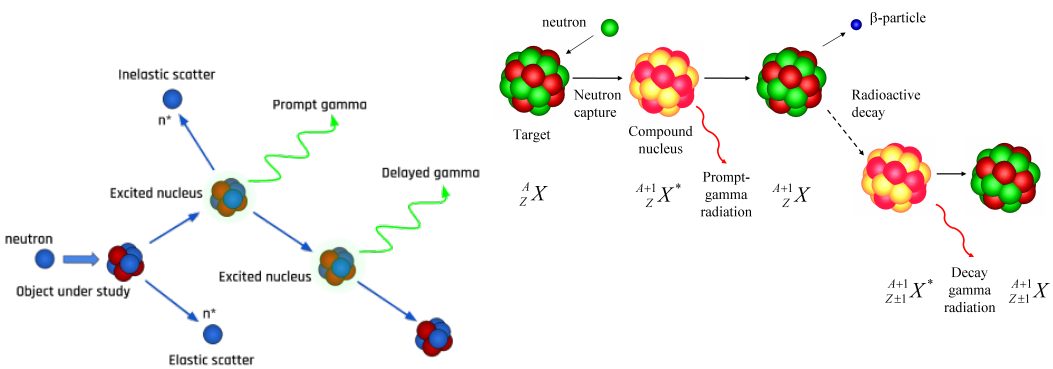

(a) Neutron scattering[15] **(b)** Neutron capture[16]

Figure 1: A schematic representation of the different neutron interactions.

Neutrons are produced as fast neutrons. They are slowed down mainly through elastic scattering interactions with atomic nuclei. However, inelastic collisions also have a small contribution to the deceleration of fast neutrons. The slowing down of fast neutrons through scattering events is called neutron moderation. Neutrons are most efficiently moderated through interactions with hydrogen because a neutron can lose up to all of its kinetic energy in a single collision with a hydrogen nucleus due to the equal masses of a proton and a neutron.

Once the fast neutrons are slowed down through (in)elastic scattering, the probability of neutron capture increases. This interaction probability is determined by the activation cross-section. The activation cross-section, as well as the cross-section of other nuclear reactions, is symbolized by the letter σ and represents the effective target area of the target nucleus when it is bombarded by a particle. The activation cross-section thus has the dimensions of area and is most commonly given in the unit barn, which is equal to 10^{-24} cm^2. In the specific case of thermal neutron capture, the activation cross-section is called the neutron capture cross-section.

The neutron capture cross-section strongly depends on energy. As neutron energies become very small, i.e. in the range of thermal energies, the neutron absorption cross-section is given by[6, 7]:

$$\sigma \propto \frac{1}{\sqrt{E}} \propto \frac{1}{v} \tag{5}$$

This relation is known as the *1/v-law*. It states that the neutron capture cross-section σ is inversely proportional to the square root of the neutron's kinetic energy E and thus inversely proportional to the velocity v of the neutron.
If the capture cross-section σ_0 at a particular energy E_0 is known, the cross-section at another energy can be obtained using the *1/v-law* in the following way[6, 7]:

$$\frac{\sigma}{\sigma_0} = \frac{v_0}{v} = \sqrt{\frac{E_0}{E}} \tag{6}$$

Depending on the type of absorbing nucleus, these equations are valid for neutron energies up to either 100 eV or 1 keV.

Neutron capture may result in the production of a radioactive isotope as is the case for example in neutron capture by ^{23}Na and ^{40}Ar. The production of a radionuclide by absorption of a neutron is called neutron activation. The induced activity of the radioactive product by neutron activation depends among others on the incoming neutron flux.

Neutron activation

In the following section, a formula is derived for calculating the effective thermal neutron flux from the detected radioactivity of isotopes produced by neutron activation. This formula was derived with the aid of books by Turner[7], Knoll[8] and Cember and Johnson[6], along with an article by Chao et al.[3] and a document written by S. Brandenburg[17].

The activity of a sample irradiated by a neutron flux can be determined by looking at the change in the number of radioactive atoms. The change in the number of radionuclides is given by the difference between the rate of production and the rate of decay. The production rate from neutron capture is given by:

$$\text{production rate} = \phi\sigma n \tag{7}$$

where

ϕ = effective neutron flux (cm^{-2}s^{-1})
σ = activation cross-section (cm^2)
n = number of target atoms

The produced radioactive atoms undergo radioactive decay resulting in the loss of radionuclides. The loss of radioactive atoms due to decay is given by:

$$\text{decay rate} = \lambda N \tag{8}$$

where N is the number of radioactive atoms present and λ is the decay constant in s^{-1}.

The decay constant is related to the half-life $t_{1/2}$ of a radionuclide by the formula:

$$\lambda = \frac{ln(2)}{t_{1/2}} \tag{9}$$

Combining Equation 7 and 8 the rate of change in N can be written as:

$$\frac{dN}{dt} = \phi\sigma n - \lambda N \tag{10}$$

Assuming the effective neutron flux ϕ and the number of target atoms n are constant, the solution to this differential equation is given by (a more elaborate derivation is given in [7]):

$$\lambda N = \phi\sigma n \left(1 - e^{-\lambda t_{irr}}\right) \tag{11}$$

This equation shows the activity ($A = \lambda N$) of the radioactive atoms as a function of irradiation time t_{irr} (in s). The term $\phi\sigma n$ is often called the *saturation activity*, since it represents the maximum obtainable activity after infinitely long irradiation times.

The number of radioactive atoms at the end of irradiation can be obtained by rewriting Equation 11. This gives the following formula:

$$N_{end\ radiation} = \frac{n\sigma\phi}{\lambda}\left(1 - e^{-\lambda t_{irr}}\right) \tag{12}$$

In the time between the end of irradiation and the start of the measurement, no new radioactive atoms are produced. However, part of the atoms are lost due to radioactive decay. This results in the number of atoms at the start of the measurement being equal to:

$$N_{start\ measurement} = N_{end\ radiation} e^{-\lambda t_1} \tag{13}$$

where t_1 (in s) is the time between the end of irradiation of the sample and the start of the measurement.

The number of gamma rays emitted by the radionuclides, which are detected by the detector, depends on several factors. First, it depends on the number of atoms decaying during the measurement, since the number of detected gamma rays is proportional to the number of atoms decayed. The number of radionuclides lost through decay is determined from the difference between the number of nuclides at the start and at the end of the measurement. Moreover, the detection depends on the efficiency of the detector, the amount of dead time and the probability that a particular gamma ray is emitted in the radioactive decay, which is called the branching ratio of the emitted gamma ray. Combining these leads to the following formula:

$$N_{detected} = I\epsilon(1-\delta)\left(N_{end\ measurement} - N_{start\ measurement}\right) \tag{14}$$

where ϵ represents the detection efficiency and the branching ratio is given by I.

Due to the finite time duration of producing a pulse by the detector, it takes some time after each event before the next event can be recorded. This time is called the dead time and is denoted by the symbol δ. It can be calculated from the real and live time corresponding to the measurement using the following formula:

$$\delta = \frac{real\ time - live\ time}{real\ time} \tag{15}$$

$N_{start\ measurement}$ is given by Equation 13 and $N_{end\ measurement}$ is given by:

$$N_{end\ measurement} = N_{start\ measurement} e^{-\lambda t_{meas}} \tag{16}$$

where t_{meas} is the measurement time (in s).

Combining Equations 13, 14 and 16 gives the number of detected gamma rays during measurement time:

$$N_{detected} = I\epsilon(1-\delta)\frac{n\sigma\phi}{\lambda}\left(1 - e^{-\lambda t_{irr}}\right)\left[e^{-\lambda t_1} - e^{-\lambda t_2}\right] \tag{17}$$

where

t_{irr} = irradiation time (s)
t_1 = time between end of irradiation and start of measurement (s)
t_2 = time between end of irradiation and end of measurement (s)
ϕ = effective neutron flux ($cm^{-2}s^{-1}$)
σ = activation cross-section (cm^2)
n = number of target atoms
λ = decay constant (s^{-1})
δ = detector dead time (%)
ϵ = detection efficiency
I = branching ratio (%)

Rewriting Equation 17 leads to the following equation for the effective neutron flux:

$$\phi = \frac{\lambda N_{detected}}{I\epsilon(1-\delta)n\sigma\left(1 - e^{-\lambda t_{irr}}\right)\left[e^{-\lambda t_1} - e^{-\lambda t_2}\right]} \tag{18}$$

In the case of multiple neutron irradiations of the same target, Equation 18 becomes:

$$\phi = \frac{\lambda N_{detected}}{I\epsilon(1-\delta)n\sigma \sum_{i=1}^{k} \left(\phi_{r,i}\left(1-e^{-\lambda t_{irr,i}}\right)\left[e^{-\lambda t_{1,i}} - e^{-\lambda t_{2,i}}\right]\right)} \tag{19}$$

where k denotes the total number of irradiations and $\phi_{r,i}$ represents the relative flux of the ith irradiation. The time intervals corresponding to the ith irradiation are denoted by $t_{irr,i}$, $t_{1,i}$ and $t_{2,i}$.

Neutron absorption

While the neutron flux passes through a target, neutrons are absorbed due to neutron capture. This leads to a reduction of the neutron flux. Therefore, the atoms "deeper" in the target are subject to a smaller effective beam flux. The reduction of the neutron flux, while passing through a slice of the target with thickness dx (in cm), is given by:

$$\frac{d\phi}{\phi} = -\mu dx \tag{20}$$

where μ represents the attenuation coefficient of the target material in cm^{-1}.

The fraction of the flux corresponding to neutrons transmitted through a target layer with thickness x can be obtained by integrating Equation 20. This yields:

$$\frac{\phi_t}{\phi_0} = e^{-\mu x} \tag{21}$$

where ϕ_t and ϕ_0 are the transmitted and initial neutron flux in (cm^{-2}s^{-1}), respectively.

For neutron capture interactions, the attenuation coefficient is given by the product of the atomic density and neutron capture cross-section σ. In the case of multiple types of atoms in a target with different cross-sections, the attenuation coefficient (in cm^{-1}) can be written as:

$$\mu = \frac{\rho}{M} N_A \sum_i k_i \sigma_i \tag{22}$$

where

ρ = density of the target material (gcm^{-3})
M = molecular weight (gmol^{-1})
N_A = Avogadro constant (6.02×10^{23} mol^{-1}[18])
k_i = number of target atoms of type i per molecule
σ_i = neutron capture cross-section corresponding to target atom of type i (cm^2)

2.3 Production and decay of relevant isotopes

As already mentioned, the products of neutron capture reactions can be radioactive isotopes. Two examples of neutron capture reactions resulting in radioactive isotopes are ^{23}Na(n,γ)^{24}Na and ^{40}Ar(n,γ)^{41}Ar. These are the reactions relevant for this research and will therefore be discussed in more detail here. The data stated in this section are obtained from articles by Firestone et al.[19, 20] and Fischer et al.[21], along with some online sources[1, 2].

^{24}Na Production and Decay

^{23}Na has a 100% abundance in natural sodium. When a neutron is added to this isotope by means of neutron capture, an excited state of the radioactive isotope ^{24}Na is formed. The probability for this neutron capture is given by the neutron capture cross-section, which in the case of thermal neutrons is equal to 0.541(3) barn.

The decay scheme of ^{24}Na is shown in Figure 2a. Once ^{24}Na is formed, it will decay by β^--emission to an excited state of ^{24}Mg. This decay has a half-life of 15 hours. Thereafter, the excited state of the ^{24}Mg decays in two steps to the stable ground state of ^{24}Mg. During this process two gamma rays with energies of 1369 and 2754 keV are emitted. The branching ratios of these gamma rays with respect to the decay of ^{24}Na are 99.99 % and 99.86 %, respectively.

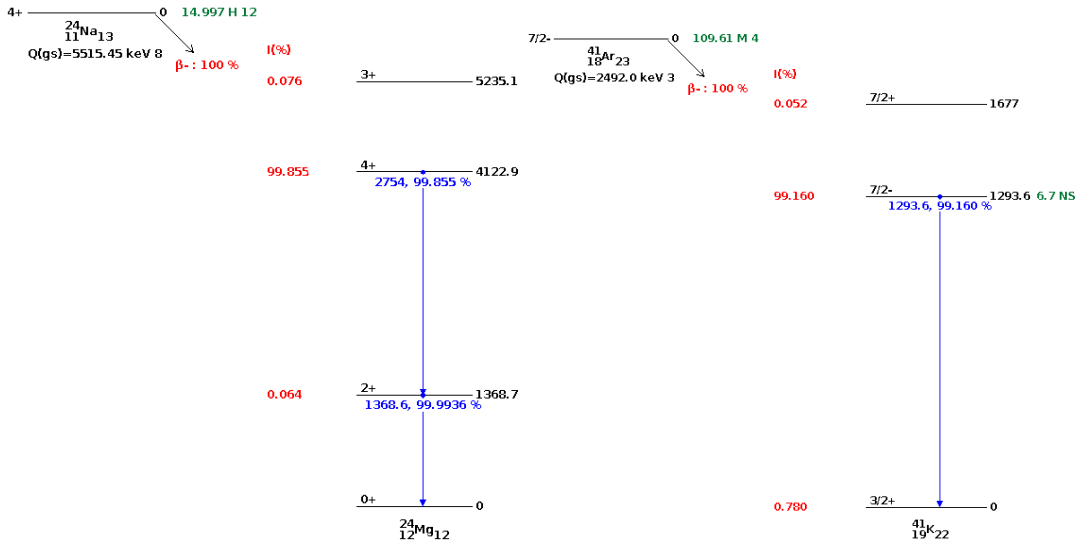

(a) Decay scheme of ^{24}Na **(b)** Decay scheme of ^{41}Ar

Figure 2: Decay schemes showing the states of the radioactive isotopes and their daughter nuclei. The half-lives of the isotopes are shown in green and the β-decay branching ratios are shown in red. The emitted gamma rays are represented by the blue arrows together with their energies and branching ratios.[2]

^{41}Ar Production and Decay

Together with nitrogen and oxygen, argon is one of the main components of standard dry air. Argon makes up 0.93% of the volume of gases in the Earth's atmosphere. From the naturally occurring argon molecules, 99.60 % is available as the isotope ^{40}Ar. When thermal neutrons hit these atoms, the neutrons are captured with a probability given by the thermal neutron capture cross-section. This neutron capture cross-section was measured by Fischer et al.[21] to be 0.673(85) barn.

The result of the neutron capture is the creation of the radioactive isotope ^{41}Ar, which has a half-life of 110 minutes. The decay scheme of ^{41}Ar is shown in Figure 2b. It decays via β^--emission to an excited state of ^{41}K, which subsequently decays to a stable state of ^{41}K. During this last decay a gamma ray with a branching ratio of

99.16 % and an energy of 1294 keV is emitted.

2.4 Radiation Detectors

During the decay of both ^{41}Ar and ^{24}Na, gamma rays are emitted. These gamma rays have to be detected in order to determine the activity of the irradiated targets. This gamma-ray detection is done with the use of a high-purity germanium (HPGe) detector located at the PARTREC facility. It is a type of semiconductor detector. Therefore, to understand the working of an HPGe detector, the basic principles of a semiconductor detector will first be explained before explaining the HPGe detector in more detail. This section is based on the books by G.F. Knoll[8] and J.C. Morrison[22] and some online resources[23–26].

Semiconductor diode detector

Semiconductor detectors are radiation detectors made of semiconductor materials like silicon and germanium. The electrons in these semiconductor materials are confined to energy bands. The lower band is called the valence band and the upper one is known as the conduction band. These bands are separated by a so-called bandgap, which in the case of a semiconductor is about 1 eV. Electrons existing in the valence band are bound to the crystal, while electrons in the conduction band are free to migrate through the crystal. In the absence of thermal energy, all electrons are in the valence band. The electrons can be excited across the bandgap to the conduction band due to thermal excitation or ionizing radiation. Due to this excitation, an electron is present in the conduction band, while at the same time a hole is left in the valence band. A so-called electron-hole pair is created. These charge carriers (i.e. electron-hole pairs) can move under the influence of an applied electric field leading to conductivity of the material.

In pure semiconductors, also known as intrinsic semiconductors, all electrons in the conduction band and holes in the valence band are created by thermal excitation (or ionizing radiation if present). Since the electrons and holes are created in pairs, the number of electrons in the conduction band is equal to the number of holes in the valence band. However, real semiconductors always contain some impurities leading to additional electrons or holes. These semiconductors are said to be doped. Impurities can be of two types. The first type are donor impurities. These add additional electrons to the conduction band leading to an n-doped crystal. The second type of impurities, acceptor impurities, result in additional holes in the valence band. Crystals containing extra holes are said to be p-doped. When an n-doped and p-doped material are brought into contact, a p-n junction is formed. A schematic of a p-n junction is shown in Figure 3.

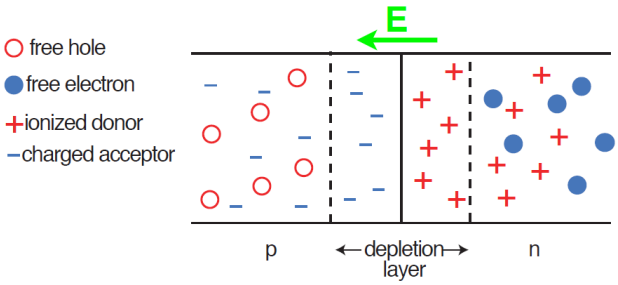

Figure 3: Schematic representation of a p-n junction.[27]

Once the n- and p-side are joined, free electrons from the n-side will start to diffuse into the p-material and recombine with holes. At the same time, holes from the p-side migrate into the n-material and recombine with electrons. A region lacking mobile charge carriers is created. This region, known as the depletion layer, contains positive donor impurities on the n-side and negative acceptor impurities on the p-side of the junction, which creates a potential barrier between the two sides. The electric field barrier prevents further diffusion of charge carriers. The size of the depletion zone can be modified by applying a bias voltage across the junction. When a reverse bias is applied, i.e. a negative voltage is applied to the p-side, electrons and holes move away from the junction resulting in an increase of the size of the depletion region. In contrast, a forward bias reduces the size of the depletion zone.

Reverse biased p-n junctions are the basis of semiconductor diode detectors. The depletion region functions as radiation detector. The principle of radiation detection of a semiconductor detector is as follows. When ionizing radiation enters the depletion region of the detector, atoms become ionized and electrons are excited from the valence to the conduction band. This leads to the creation of electron-hole pairs. The number of generated electron-hole pairs is proportional to the energy deposited by the incident radiation. Due to the electric field across the depletion region, the created electrons will move towards the n-type material, while the holes will move towards the p-side, resulting in an electrical signal or pulse. This pulse is detected and gives information about the energy of the incident radiation. The number of pulses is a measure of the intensity of the radiation.

High-purity germanium (HPGe) detector

One type of semiconductor detectors are germanium-based semiconductor detectors. They are commonly used for gamma-ray spectroscopy due to their high energy resolution. Germanium has a high atomic number resulting in a high probability for gamma-ray interaction in the detector. Moreover, the average energy needed for the creation of an electron-hole pair is 2.9 eV. This is smaller than the average energy for other semiconductor materials like for example silicon, which has an average ionization potential of 3.6 eV. Therefore, a better energy resolution is achieved with the use of germanium-based detectors compared to other semiconductor detectors. On the other hand, the energy band gap between the valence band and conduction band is very low for germanium namely 0.67 eV. Consequently, thermal excitation is dominant at room temperature. Therefore, to reduce generation of charge carriers due to thermal excitation leading to leakage current, germanium-based detectors must be cooled. This

is often done using liquid nitrogen as a cooling medium, which has a temperature of 77 K. Cooling with liquid nitrogen reduces thermal excitation of valence electrons such that electron-hole pairs can only be generated by ionizing radiation.

Germanium detectors are semiconductor diode detectors with a p-i-n structure. This means that the detector consists of an intrinsic or depleted region, which is sensitive to ionizing radiation, surrounded by an n-type material on one side and a p-type material on the other side. Using germanium detectors with normal purity, depletion regions with thicknesses of a few millimeters can be achieved. However, to fully absorb high-energy gamma rays up to a few MeV, depletion depths of several centimeters are needed. The thickness of the depletion layer, when a reverse bias voltage is applied, is given by:

$$d = \left(\frac{2\epsilon V}{eN}\right)^{1/2} \tag{23}$$

where

V = reverse bias voltage (V)
N = net impurity concentration in the semiconductor material (m^{-3})
ϵ = dielectric constant (Fm^{-1})
e = electronic charge (C)

The net impurity concentration thus has to be reduced as much as possible to obtain the largest depletion region. Germanium with low impurity concentrations as low as 10^{10} atoms cm^{-3} can be produced. Germanium-based detectors manufactured from this high-purity germanium are called high-purity germanium (HPGe) detectors. These detectors have depletion regions of several centimeter thickness. Therefore, they can be used to detect high-energy photons up to a few MeV like for example the photons emitted during the decay of ^{41}Ar and ^{24}Na.

2.5 Pulse-height spectrometry

In this research, pulse-height spectrometry is used to study the signals obtained from the HPGe detector and to determine the gamma rays emitted by radioactive isotopes like ^{24}Na and ^{41}Ar. This section discusses the general components visible in pulse-height spectra. It has been written with the aid of the books by Knoll[8] and Cherry et al.[10]. Additionally, some online resources were used [28–32].

Pulse-height spectra

A pulse-height spectrum shows the number of radiation events detected, also called counts, versus the amplitude of the signal from the detector corresponding to those events. This amplitude is not necessarily the full energy of the incoming photon. However, it reflects the amount of energy deposited in the detector by the events, which might be equal to or less than the full energy of the incoming photon. The amount of energy deposited in the detector depends on the type of interaction between the incident photon and the detector material. Photons mainly deposit their energy via the photoelectric effect, Compton scattering or pair-production. Possible interaction

trajectories in a radiation detector for each of these interaction mechanisms are shown in Figure 4.

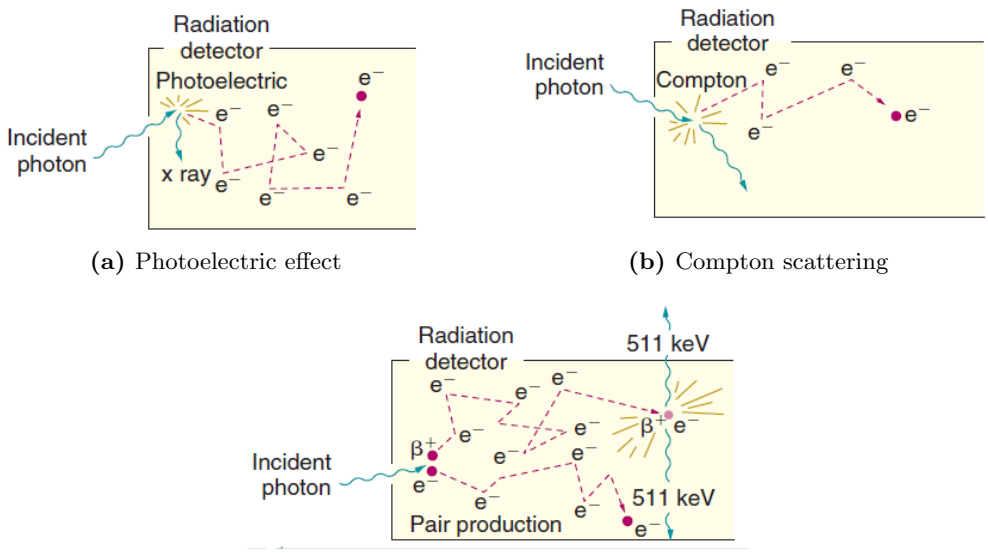

(a) Photoelectric effect

(b) Compton scattering

(c) Pair production

Figure 4: Possible interaction trajectories for photons in a radiation detector.[10]

In these interactions, the incident photon loses (part of) its energy to a photoelectron, recoil electron or positron-electron pair, respectively. These electrons transfer their energy to the detector via secondary ionization events. The remaining part of the incident photon's energy is converted into secondary photons. These secondary photons can be characteristic X-rays, scattered photons or annihilation photons depending on the type of interaction.

In the case of photoelectric absorption, the incident photon is totally absorbed by the atom. Its energy is transferred to a photoelectron, which is ejected from the atom leaving a vacancy in an orbital electron shell. This vacancy is filled by capture of a free electron or rearrangement of electrons from other shells, which leads to the emission of characteristic X-rays or Auger electrons.

In Compton scattering, the incident photon is not absorbed. Instead, it is deflected through a scattering angle θ, while transferring part of its energy to the recoil electron. The energy transferred to the electron depends on the scattering angle. The energy of the scattered photon (in MeV) is given by:

$$E_{sc} = \frac{E_0}{1 + \frac{E_0}{0.511}(1 - cos(\theta))} \tag{24}$$

where E_0 is the energy of the incident photon (in MeV) and θ represents the scattering angle.

By considering conservation of energy, the energy of the recoil electron E_{re} can be

written as:

$$E_{re} = E_0 - E_{sc} \tag{25}$$

The energy of the recoil electron ranges from small values for small scattering angles to a maximum value. The maximum energy transferred to the recoil electron, which corresponds to the minimum energy of the scattered photon, is obtained for a scattering angle of 180°.

When the incident photon energy exceeds twice the rest-mass energy of an electron (1.022 MeV), pair-production might occur. The incident photon disappears and generates an electron-positron pair. Subsequently, the electron and positron dissipate their energy in the detector material via ionization and excitation events. Once the positron has slowed down, it recombines with an electron. The result is the emission of two annihilation photons with an energy of 0.511 MeV in opposite directions.

These secondary photons present in the different interaction mechanisms might deposit their energy in the detector. However, they can also escape from the detector. In the latter case, less than the full energy of the incident photon is detected.

Pulse-height spectra contain general features due to the different interaction mechanisms of the gamma rays with the detector. Some of these features are illustrated in Figure 5. Detection of the full gamma-ray energy results in a peak at the energy of the incoming photon. This full-energy peak is called the photopeak. Most of the photoelectric interactions lead to a pulse in the photopeak. Compton interactions and pair-production events also contribute to the photopeak, when the secondary photons are fully absorbed in the detector. However, other characteristics appear in the spectrum when the secondary photons escape from the detector.

One of these is the Compton region. This region is formed by detection of only the recoil electron after escape of the Compton scattered photon from the detector. Since the recoil electron has a range of energies depending on the scattering angle, the Compton region ranges from near zero to the maximum energy of the recoil electron. At this maximum value the Compton region ends with a sharp edge known as the Compton edge. In-between the photopeak and the Compton edge, signals are detected corresponding to multiple Compton scattering events.

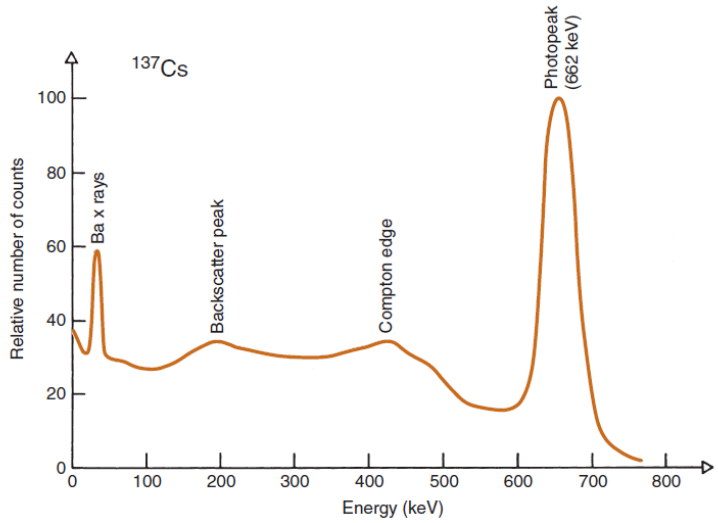

Figure 5: A pulse-height spectrum obtained from a ^{137}Cs source showing the Compton region, Compton edge and photopeak.[10]

In addition to the photopeak, a single and double escape peak may appear in the spectrum. These peaks are illustrated in Figure 6. When the incident photon interacts with the detector via pair-production, annihilation photons with an energy of 0.511 MeV are produced. These can escape the detector. If only one of the two annihilation photons escapes, the event is recorded in the single escape peak. If both photons escape, a pulse is counted in the double escape peak. The single and double escape peak are shown at energies of 0.511 and 1.022 MeV below the photopeak, respectively.

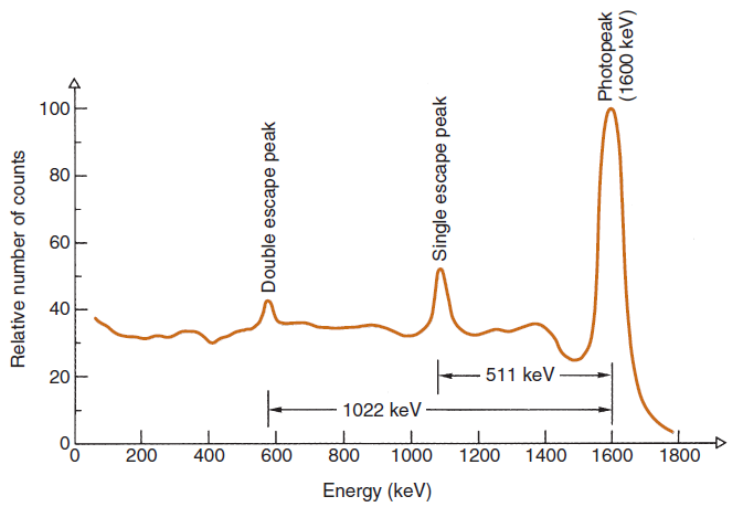

Figure 6: A pulse-height spectrum for an incident photon with an energy of 1600 keV. The single and double escape peaks are the result of the escape of one or both annihilation photons after pair-production.[10]

When two or more gamma rays are emitted by a radionuclide within the resolving time of the detector, coincidence summing can occur. This means that both gamma rays are detected simultaneously by the detector. If the full energy of both photons is

detected, this results in a so-called sum peak in the pulse-height spectrum. This sum peak has an energy equal to the sum of the separate gamma-ray energies. If one or both photons are not fully detected, the pulse is not counted in the sum peak. Instead, these pulses lead to a continuum in the spectrum.

Besides these different features, background radiation is also present in pulse-height spectra. The origin of background radiation and their effect on the spectra will be discussed in the next section.

Background radiation

During the birth and death of stars, billions of years ago, radioactive isotopes were released. Some of these radioactive isotopes are still present in the Universe due to their long half-lives. These elements are thorium-232, uranium-238 and potassium-40. These isotopes are naturally present in the Earth's crust.

Due to disintegration of the thorium and uranium nuclei, other radioactive elements with shorter half-lives are formed. The decay chains of ^{232}Th and ^{238}U are shown in Figure 7. The presence of uranium, thorium and their daughter isotopes gives rise to gamma radiation originating from the Earth's ground. This so-called telluric radiation is a major source of background radiation.

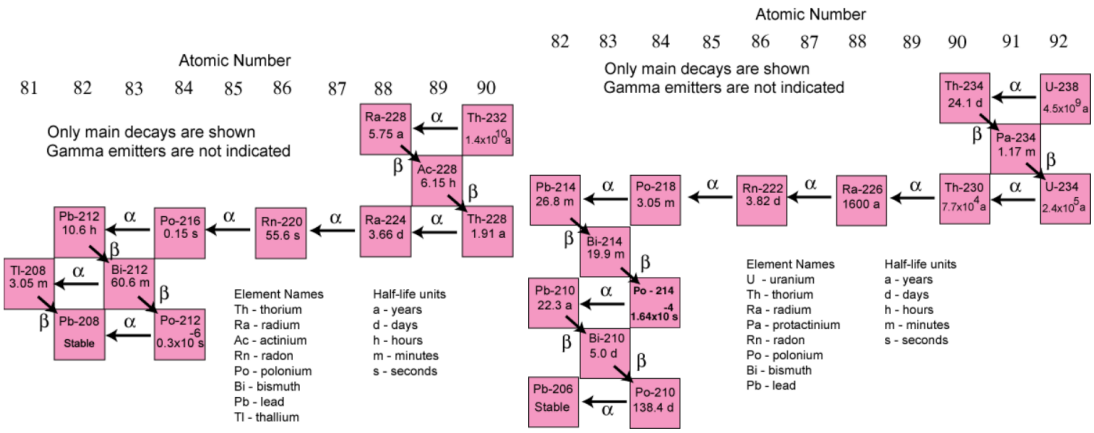

(a) Thorium-232 [30] **(b)** Uranium-238 [31]

Figure 7: Decay chains of two naturally occurring radioactive isotopes.

As can be seen in Figure 7b, ^{222}Rn is one of the daughter isotopes in the decay chain of ^{238}U. When ^{226}Ra decays by the emission of an α-particle, ^{222}Rn is formed. Since its half-life is 3.8 days, the produced radon can escape the surface of rocks containing uranium resulting in radioactivity in the air. Since ^{222}Rn exists in a gaseous state, it is the main contributor to natural radioactivity for humans in daily life.

These sources of natural radioactivity cause the appearance of background radiation peaks in pulse-height spectra. To be able to identify these peaks, the gamma rays with the highest intensities in the decay chains of ^{232}Th and ^{238}U are listed in Table 1.

Moreover, the emitted gamma-ray energy corresponding to the decay of ^{40}K is stated.

Table 1: Energies of the most intense gamma rays emitted by naturally occurring radioactive isotopes.[32]

	Parent isotope	Gamma-ray energy (keV)
^{232}Th	^{228}Ac	338.3 911.2 969.0
	^{212}Pb	238.6
	^{212}Bi	727.4
	^{208}Tl	583.2 2614.5
^{238}U	^{214}Pb	295.2 351.9
	^{214}Bi	609.3 1120.3 1764.5
^{40}K		1460.8

2.6 Summing correction

^{24}Na emits two gamma rays with energies of 1369 and 2754 keV. Coincidence summing can occur, if both of these gamma rays are detected simultaneously by the detector. When both photons are fully detected in coincidence, a count is added to the sum peak in the pulse-height spectrum, which has an energy of 4123 keV. One photon can also be detected in coincidence with part of the energy of the second photon. Both of these events result in the removal of pulses from the full-energy photopeaks. Therefore, coincidence summing leads to a decrease in the efficiency for detecting the full-energy gamma rays. To compensate for this decrease in efficiency, coincidence summing correction factors have to be calculated. Formulas for the correction factors are derived below with the use of the book by Debertin and Helmer[33].

The correction factor for the first gamma ray, i.e. 2754 keV, can be derived by considering the count rates in both the presence and absence of coincidence summing. When coincidence summing is absent, the count rate in the full-energy peak n_{p1} of the 2754 keV gamma ray is given by:

$$n_{p1} = Ap_1\epsilon_{p1} \tag{26}$$

where

A = activity of ^{24}Na
p_1 = emission probability of the 2754 keV gamma ray
ϵ_{p1} = full-energy peak efficiency of the 2754 keV gamma ray

However, in the presence of coincidence summing, the count rate in the full-energy peak is smaller since simultaneous detection of the gamma rays could happen. Simultaneous detection results in a pulse at a different energy than the photopeak and thus decreases

the pulse rate in the full-energy peak. The probability that the first gamma ray is detected simultaneously with (part of) the second gamma ray is equal to the product of the probability of detecting the first gamma ray and the total detection efficiency of the second gamma ray ϵ_{t2}. Therefore, in the presence of summing, the count rate in the full-energy peak $n_{p1,s}$ is given by:

$$n_{p1,s} = Ap_1\epsilon_{p1} - Ap_1\epsilon_{p1}\epsilon_{t2} = Ap_1\epsilon_{p1}\left(1 - \epsilon_{t2}\right) \tag{27}$$

The efficiency corrected for coincidence summing is calculated by dividing the full-energy peak efficiency by the correction factor, which is given by:

$$C_1 = \frac{n_{p1}}{n_{p1,s}} = \frac{1}{1 - \epsilon_{t2}} \tag{28}$$

.

In a similar manner, the correction factor for the efficiency of detecting the second gamma ray, i.e. 1369 keV, can be derived. The correction factor C_2 depends only on the total detection efficiency of the first gamma ray ϵ_{t1} and is given by:

$$C_2 = \frac{1}{1 - \epsilon_{t1}} \tag{29}$$

3 Methods

3.1 Am-Be neutron source

The experiments performed for the purpose of this research are related to neutron activation. The neutron activation of several samples was accomplished with the use of a neutron source located at the PARTREC facility. The neutron source consisted of an Am-Be source contained within a solid cube made of paraffin. Paraffin is a hydrogenous material which is used as neutron moderator. Fast neutrons emitted by the Am-Be source are slowed down to thermal energies due to elastic scattering events in the paraffin. The paraffin thus functions as a source of thermalized neutrons.

The Am-Be source inside the paraffin cube is a radioactive neutron source consisting of an alpha-emitting material, americium, and a light metal, beryllium. The alpha particles produced by ^{241}Am react with ^{9}Be through an (α,n) reaction, which results in the production of ^{12}C and the emission of neutrons. The neutron intensity of the source depends on the half-life of the alpha emitter, which for ^{241}Am is equal to 432.6 years [2]. The activity of ^{241}Am in the Am-Be source was measured to be 18.5 GBq in the year 1974 [34]. This means that the activity of ^{241}Am at the time of this research (2021) was 17.2 GBq. A continuous energy spectrum of neutrons is emitted by the source, since the alpha particles are slowed down by different amounts before hitting a beryllium nucleus. The average neutron energy emitted in this reaction is 4.2 MeV [35]. The neutron energy spectrum corresponding to an Am-Be source is shown in Figure 8. As can be seen in the figure, the Am-Be source emits neutrons up to maximum energies of about 10 MeV [35]. [7, 8]

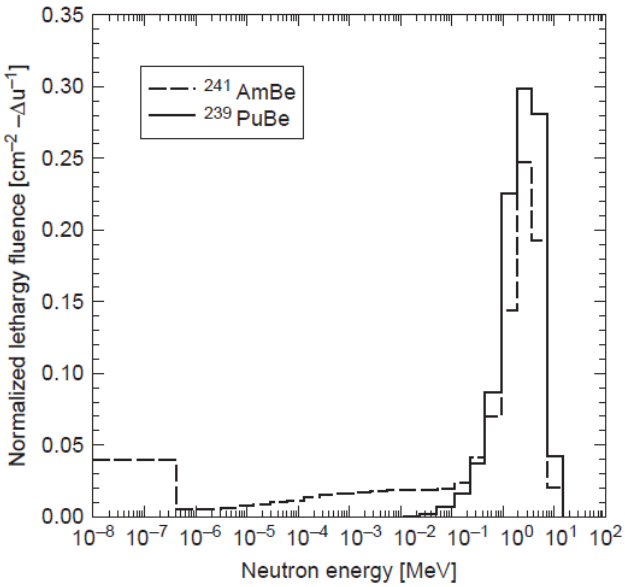

Figure 8: The normalized neutron fluence as a function of neutron energy corresponding to a ^{241}Am-Be source is shown by the dashed line.[36]

3.2 Comparison of neutron-activated $NaHCO_3$ and NaCl samples

For indirect measurement of the ^{41}Ar production, sodium can be used. Two easily obtainable substances containing sodium are $NaHCO_3$ and NaCl. To determine whether $NaHCO_3$ or NaCl could best be used to determine the neutron flux, two plastic containers with a volume of 50 ml were filled with either $NaHCO_3$ or NaCl.

Initially, the mass of these samples was determined in order to calculate the number of Na atoms present in the samples, which is needed eventually for determining the effective neutron flux. The mass fraction of sodium in the $NaHCO_3$ is equal to one fourth as stated by the manufacturer. Once the mass of the sodium is known, the number of ^{23}Na atoms, N_{Na}, can be calculated with the following formula:

$$N_{Na} = \frac{m_{Na} \times a}{M_{Na}} \times N_A \tag{30}$$

where

m_{Na} = mass of sodium (g)
a = isotopic abundance of ^{23}Na (100% [2])
M_{Na} = atomic weight of Na (22.99 gmol^{-1}[37])
N_A = Avogadro constant (6.02×10^{23} mol^{-1}[18])

For the NaCl samples, the number of ^{23}Na atoms as a function of the mass of the sample, m, is given by:

$$N_{Na} = \frac{m \times a}{M_{NaCl}} \times N_A \tag{31}$$

where M_{NaCl} is the atomic weight of NaCl, which is equal to 58.44 gmol^{-1}[37].

The $NaHCO_3$ and NaCl samples were separately neutron-activated by irradiation in the Am-Be neutron source. A schematic of this neutron source is shown in Figure 9.

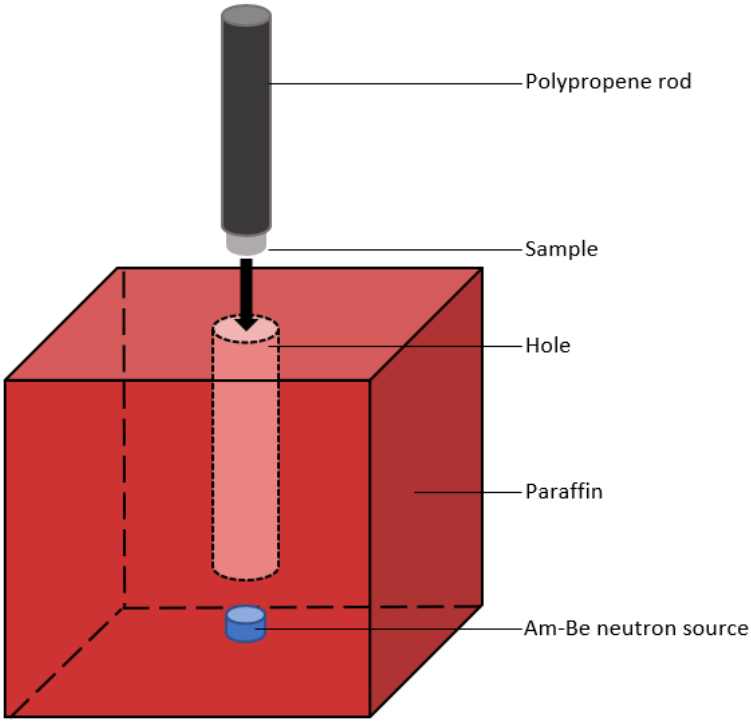

Figure 9: Schematic diagram of the Am-Be neutron source within the paraffin assembly. The polypropene rod with a sample attached on top is installed upside down inside the neutron source.

First, the $NaHCO_3$ or NaCl sample was mounted on a polypropene rod. This rod was placed upside down inside the neutron source such that the sample was as close as possible to the actual Am-Be source. The polypropene rod sealed the hole of the neutron source, which would otherwise exist towards the top of the paraffin assembly, as shown in Figure 9. Since polypropene is a hydrogenous material, just as paraffin, it also functions as neutron moderator.

The sample was irradiated for approximately two days in order to reach a ^{24}Na activity close to the saturation value (see Equation 11). During the irradiation, ^{24}Na is produced by thermal neutron activation of ^{23}Na. After irradiation, the $NaHCO_3$ or NaCl sample was taken out of the neutron source and placed on a HPGe detector to measure the gamma-ray spectrum emitted by the sample. The HPGe detector was enclosed by thick lead shielding to minimize the detection of natural background gamma radiation. The pulse-height spectra were obtained with the use of the multichannel analyzer software MAESTRO. With the use of MAESTRO, the net number of counts, i.e. the number of counts minus the background, in the several photopeaks corresponding to the decay of ^{24}Na was determined. Moreover, the net area of the sum peak was obtained. Eventually, the effective neutron flux incident on the ^{23}Na atoms in the samples was calculated.

3.3 Thermal neutron absorption

To establish the difference in thermal neutron absorption by NaCl and $NaHCO_3$, two different targets were neutron-activated in the Am-Be neutron source. Schematic diagrams of these targets are shown in Figure 10. The targets consisted of a plastic container of 50 ml filled with $NaHCO_3$, which was placed inside a larger container of 100 ml. The empty layer, with a thickness of 1 cm, surrounding the smaller container was filled with either $NaHCO_3$ or NaCl for the different targets.

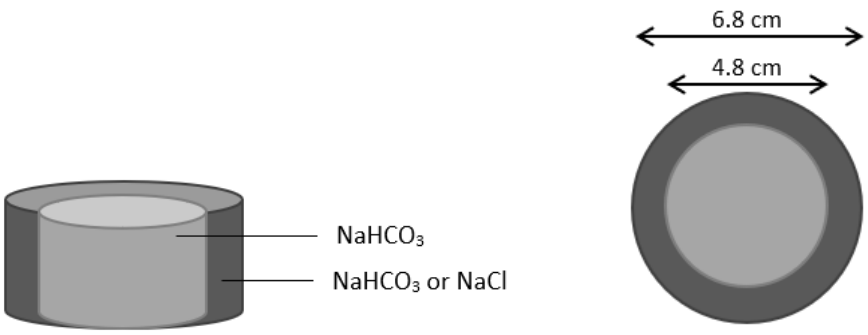

Figure 10: Schematic diagrams of the samples used in the thermal neutron absorption experiment. A side view (left) and top view (right) are shown indicating the contents and dimensions of the plastic containers.

These samples were attached to the polypropene rod and placed inside the neutron source for irradiation one after the other. After irradiation, the inner target containing $NaHCO_3$ was taken out of the sample and placed on the HPGe detector for measurement of the gamma-ray spectrum. Afterwards, the outer layer of $NaHCO_3$ or NaCl, depending on the sample, was poured from the 100 ml container into a 50 ml container and placed on the detector. This way the spectra corresponding to the outer layers of $NaHCO_3$ and NaCl were also measured. The net area of counts in the photopeaks corresponding to the gamma rays of ^{24}Na were determined for each of the obtained gamma-ray spectra. Afterwards, the effective neutron fluxes were calculated and compared.

3.4 Neutron activation of Argon pressure can

To be able to compare the obtained neutron fluxes for the $NaHCO_3$ and NaCl samples with the neutron flux incident on argon, an argon 5.0 pressure can, i.e. a can containing argon with a purity of 99.999%, was neutron-activated by the same Am-Be source. The can had a volume of 1 l and was made of aluminium. The argon was contained at a pressure of 12 bar.[38]

An equation for the concentration of ^{40}Ar atoms in the bottle or in air can be derived from the ideal gas law. The ideal gas law relates several properties of a gas and is given by[39]:

$$pV = Nk_BT \tag{32}$$

where

p = pressure (Pa)
V = volume (m^3)
N = number of atoms
k_B = Boltzmann constant = 1.38×10^{-23} JK^{-1}[18]
T = temperature (K)

To obtain the concentration of ^{40}Ar, the fraction of ^{40}Ar molecules, f_{Ar}, in the bottle or air should be included in the formula. Rewriting the ideal gas law and including f_{Ar} leads to a formula for the ^{40}Ar concentration (in m^{-3})[3]:

$$n_{Ar} = \frac{N}{V} = \frac{p}{k_B T} \times f_{Ar} \tag{33}$$

The Ar bottle was placed inside the neutron source and irradiated. The striking neutrons result in the activation of the contained ^{40}Ar atoms. Moreover, the aluminium container will also be activated, since ^{27}Al atoms can undergo multiple neutron activation reactions. These reactions result in the production of several radioactive products, which decay by the emission of gamma rays. Some of these neutron capture reactions are described below.

The first neutron activation reaction is radiative neutron capture. In this reaction a neutron is added to ^{27}Al. This results in ^{28}Al, which has a half-life of 2.2 minutes. It β-decays to an excited state of ^{28}Si, which subsequently de-excites via the emission of a gamma ray. This reaction is shown below:

$$^{27}\mathrm{Al} + \mathrm{n} \longrightarrow {}^{28}\mathrm{Al} \longrightarrow {}^{28}\mathrm{Si} + \gamma(1779\,\mathrm{keV}) \tag{34}$$

Another activation reaction of aluminium leads to the capture of a neutron and emission of a proton. The product of this reaction is ^{27}Mg, which β-decays to the first and second excited state of ^{27}Al. The half-life corresponding to this β-decay is 9.5 minutes. These excited states de-excite to the ground state by the emission of a 844 keV gamma ray with a branching ratio of 71% or by the emission of a 1015 keV gamma ray with a branching ratio of 29%.

$$^{27}\mathrm{Al}(\mathrm{n},\mathrm{p})^{27}\mathrm{Mg} \longrightarrow {}^{27}\mathrm{Al} + \gamma(844\,\mathrm{keV}\text{ or }1015\,\mathrm{keV}) \tag{35}$$

Moreover, an α-particle or two neutrons can be produced after neutron capture in ^{27}Al. This results in the two reactions shown below. The first reaction shows the production of ^{24}Na, which decays with the emission of two gamma rays. The decay information corresponding to this reaction was already mentioned in Theory subsection 2.3. In the second reaction, either a ground state of ^{26}Al, with a half-life of 7.4×10^5 years, or an isomeric state of ^{26}Al, with a half-life of 6.3 s, is produced. The ground state of ^{26}Al decays to ^{26}Mg while emitting 1809 keV gamma rays. When the isomeric state is produced, it also decays to the ground state of ^{26}Mg. However, no gamma rays are emitted during this decay except for annihilation photons.

$$^{27}\mathrm{Al}(\mathrm{n},\alpha)^{24}\mathrm{Na} \longrightarrow {}^{24}\mathrm{Mg} + \gamma(1369\,\mathrm{keV}\text{ and }2754\,\mathrm{keV}) \tag{36}$$

$$^{27}\mathrm{Al}(\mathrm{n},2\mathrm{n})^{26}\mathrm{Al} \longrightarrow {}^{26}\mathrm{Mg} + \gamma(1809\,\mathrm{keV}) \tag{37}$$

The neutron capture cross-sections corresponding to these ^{27}Al(n,x) reactions are shown in Figure 11. [40, 41]

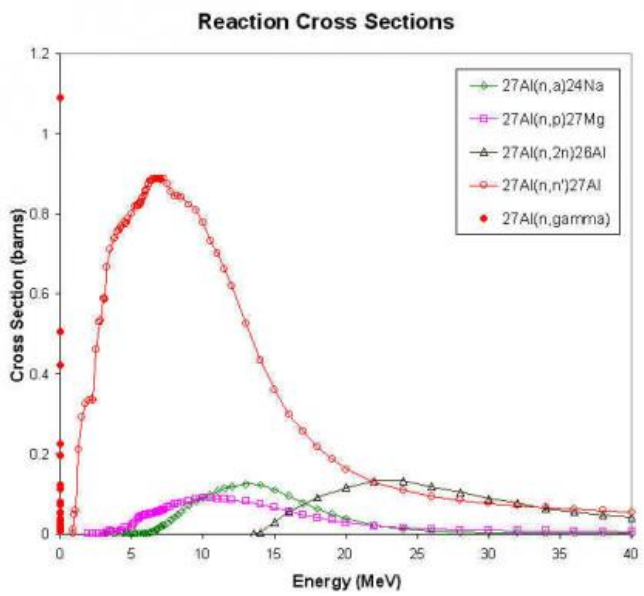

Figure 11: Neutron capture cross-sections for the ^{27}Al(n,x) reactions as a function of neutron energy.[41]

The capture cross-sections of the several aluminium activation reactions as a function of neutron energy can be compared with the neutron energies emitted by the Am-Be source, as shown in Figure 8. From this comparison it can be concluded that the ^{27}Al(n,α)^{24}Na, ^{27}Al(n,p)^{27}Mg and ^{27}Al(n,γ)^{28}Na reactions are expected to take place, when the argon bottle is placed inside the neutron source.

Although part of the neutrons incident on the gas container are captured by the aluminium wall, the aluminium will hardly influence the thermal neutron flux incident on the ^{40}Ar contained in the gas bottle. Combining the thickness, height and diameter of the aluminium wall, which are respectively 0.6, 260 and 75 mm, with the empty mass of 113 g of the gas container [38, 42], the atomic density of ^{27}Al in the wall was calculated to be 6.1×10^{22} atoms cm^{-3}. Substituting this atomic density, the neutron capture cross-section of ^{27}Al (0.23 barn [2]) and the aluminium wall thickness into Equation 22 and 21 yields a value of 0.999 for the fraction of neutrons transmitted through the aluminium wall. From this value, it can be concluded that the thermal neutron flux incident on the argon atoms in the gas container will not be significantly reduced by the presence of the aluminium wall.

After irradiation and activation of the argon pressure can, the Ar bottle was placed on the HPGe detector to obtain the pulse-height spectrum. Since the can was too large for the detector, the lid of the lead shielding construction enclosing the detector could not be closed during the measurement. This caused extra background radiation in the obtained spectrum. From the obtained spectrum the number of detected gamma rays in the photopeak corresponding to the decay of ^{41}Ar were determined and used

to calculate the effective neutron flux incident on the argon gas bottle. Finally, this effective neutron flux was compared to the neutron fluxes obtained for the $NaHCO_3$ and NaCl samples.

3.5 Neutron flux distribution

The argon bottle and sodium samples have heights of 26 and 3.85 cm, respectively. Due to this relatively large difference in geometry, the neutron activation depends significantly on the neutron flux distribution in the neutron source. Therefore, to make a good comparison between the obtained neutron fluxes, corresponding to the argon container and sodium samples, the neutron flux distribution of the neutron source should be determined.

To obtain an indication of the neutron flux distribution as a function of height in the neutron source, multiple containers were stacked on top of a rod made of polypropene. Two piles of containers were made with different configurations. Images and schematics of these are shown in Figure 12. Both stacks consisted of alternating empty and $NaHCO_3$ filled containers with a total of six or seven plastic containers. The sample numbers corresponding to the $NaHCO_3$ containers are shown in the schematics[1].

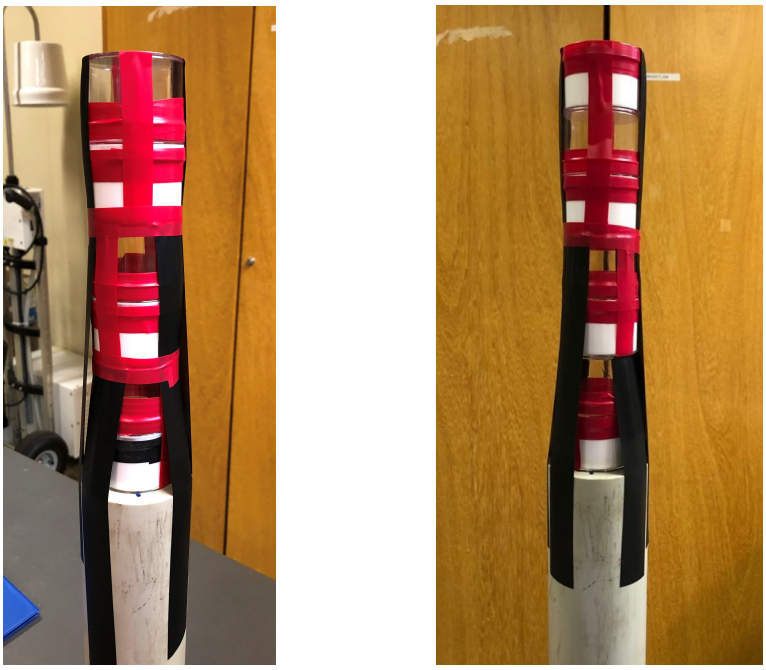

(a) **(b)**

[1] Two piles consisting of alternating empty and filled containers were used instead of one pile with all containers filled with $NaHCO_3$ such that the gamma-ray spectra did not have to be measured all at once.

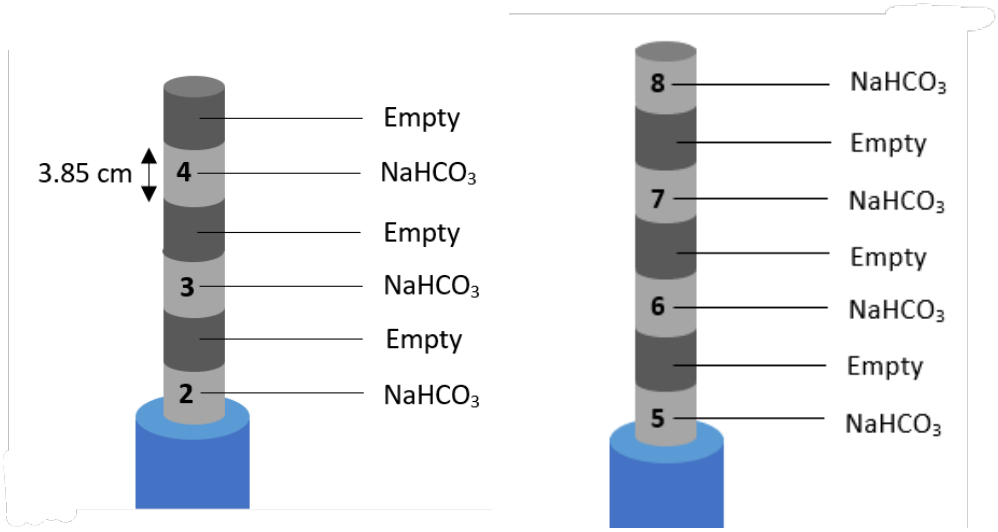

(c) (d)

Figure 12: Images of the stacks of plastic containers (a,b) used for the measurements of the neutron flux distribution and the corresponding schematics (c,d). The height and content of the containers are listed in the schematic figures. The containers, filled with $NaHCO_3$, are indicated by the corresponding sample numbers.

First, one of the stacks was attached to the polypropene rod and placed upside down in the neutron source for irradiation. After almost two days of irradiation, the rod was taken out of the neutron source. Subsequently, the samples were placed on the HPGe detector one at a time to measure the gamma-ray spectra of each of the samples individually. From the measured spectra, the net area of counts in the two highest intensity peaks, corresponding to the decay of ^{24}Na, was determined. Afterwards, the same experiment was conducted for the other stack. Since the rod was inserted into the neutron source upside down, the samples with number 4 and 8 were closest to the Am-Be neutron source, while sample number 5 was furthest away. From the determined counts in the peaks, the neutron fluxes corresponding to each sample could be calculated. Comparing the neutron fluxes for the different samples yielded a neutron distribution as a function of height.

3.6 $NaHCO_3$ irradiation at GPTC

To estimate the amount of ^{41}Ar produced at the proton therapy center, eight $NaHCO_3$ samples were activated at the GPTC. These samples were located both in one of the treatment rooms and in the cyclotron bunker to measure the neutron flux at different locations. A floor map of the GPTC indicating the exact positions of the $NaHCO_3$ samples is shown in Figure 13. Sample 1 was placed inside the treatment room close to the patients, while sample 2 was located on the other side of the room inside a closet. Samples 3 to 8 were distributed across the cyclotron bunker. Samples 4 to 6 were positioned close to the beam line. More specifically, sample 4 and 5 were placed on the floor in the vicinity of the energy degrader and the energy selection system (ESS), respectively. Close to the position where the proton beam is diverted into treatment

room 1, sample 6 was placed. On the other hand, samples 3 and 7 were located away from the beam line near the entrance and exit maze. Finally, $NaHCO_3$ sample 8 was placed in a corner of the cyclotron bunker close to the concrete walls.

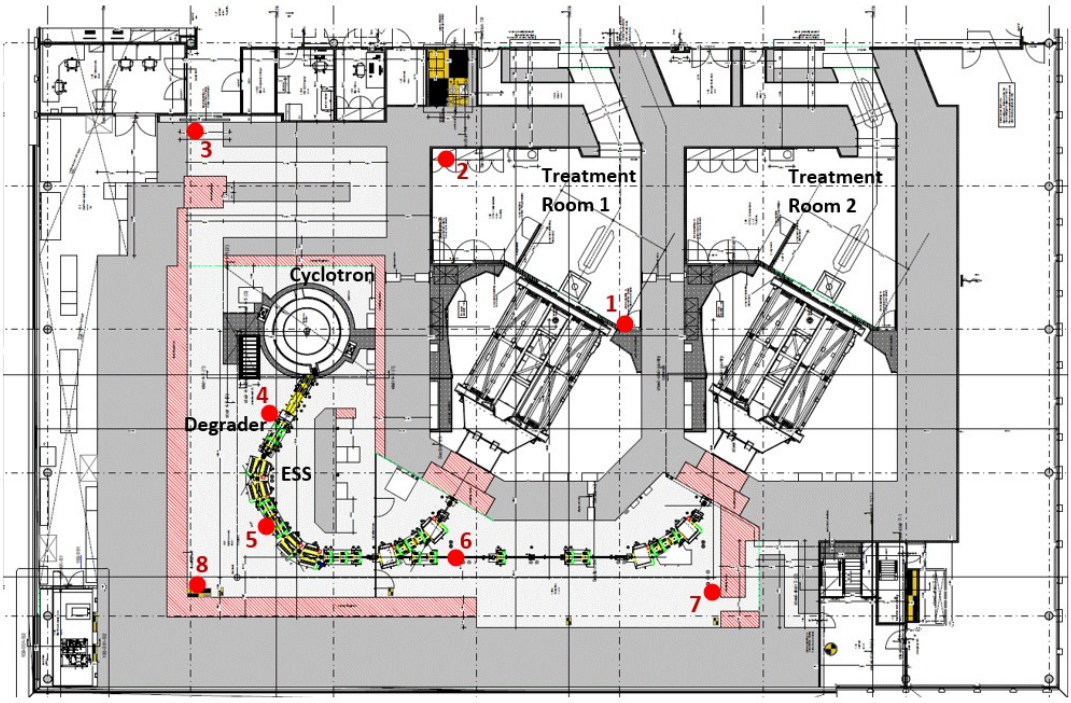

Figure 13: Floor map of the Groningen Proton Therapy Center (GPTC) showing the treatment rooms and cyclotron bunker retrieved from Marc-Jan van Goethem[2]. The red dots indicate the positions of the $NaHCO_3$ samples with their corresponding sample number. The cyclotron, degrader and energy selection system (ESS) are also indicated [43].

The samples were installed in the morning. After a full day of patient irradiations, the samples were collected and transported to the PARTREC facility. At the PARTREC facility, the gamma-ray spectra corresponding to the irradiated samples were measured. This was done using two HPGe detectors instead of one to be able to measure the gamma-ray spectra of each sample as soon as possible after the last irradiation at the GPTC. Samples 3-5, 7 and 8 were measured with HPGe detector 1. HPGe detector 2 was used for measuring samples 1,2 and 6. Subsequently, the number of counts in the photopeaks at 1369 keV were determined from the obtained spectra and used to calculate the effective neutron flux incident on each $NaHCO_3$ sample during proton irradiation. Finally, the determined effective neutron fluxes were used to determine the amount of ^{41}Ar produced at the locations corresponding to the different samples.

Calibration second HPGe detector

As already mentioned, a second HPGe detector was used to obtain the gamma-ray spectra of the $NaHCO_3$ samples irradiated at the GPTC. However, the detection ef-

[2] Department of Radiation Oncology, University Medical Center Groningen, University of Groningen, Groningen, Netherlands.

ficiencies corresponding to this second detector were unknown. These efficiencies can be calibrated using the known efficiencies corresponding to the first HPGe detector. This calibration was performed by measuring the gamma-ray spectrum of an irradiated $NaHCO_3$ sample on both HPGe detectors. From Equation 17 it can be seen that the ratio between the number of gamma rays detected by the two detectors is given by:

$$\frac{N_{det1}}{N_{det2}} = \frac{\epsilon_1(1-\delta_1)}{\epsilon_2(1-\delta_2)} \times \frac{e^{-\lambda t_{11}} - e^{-\lambda t_{21}}}{e^{-\lambda t_{12}} - e^{-\lambda t_{22}}} \tag{38}$$

where

$N_{det1,2}$ = number of detected gamma rays in detector 1 or 2
$\epsilon_{1,2}$ = detection efficiency of HPGe detector 1 or 2
$\delta_{1,2}$ = dead time of detector 1 or 2 (%)
λ = decay constant (s^{-1})
$t_{11,12}$ = time between end of irradiation and start of measurement for detector 1 or 2 (s)
$t_{21,22}$ = time between end of irradiation and end of measurement for detector 1 or 2 (s)

Rewriting this equation yields an equation for the efficiency of HPGe detector 2 (ϵ_2) as a function of the efficiency of HPGe detector 1 (ϵ_1):

$$\epsilon_2 = \frac{N_{det2}}{N_{det1}} \times \frac{\epsilon_1(1-\delta_1)}{(1-\delta_2)} \times \frac{e^{-\lambda t_{11}} - e^{-\lambda t_{21}}}{e^{-\lambda t_{12}} - e^{-\lambda t_{22}}} \tag{39}$$

4 Results & Discussion

4.1 Efficiency detector

To determine the neutron flux from the number of detected photons, the detection efficiencies of the HPGe detector are needed for the gamma rays emitted by ^{24}Na in the several samples. The gamma-ray detection efficiencies for NaCl and $NaHCO_3$ in 50 ml pill boxes were obtained by E.R. van der Graaf in [44] with the use of Monte Carlo simulations. As mentioned in [44], the relative uncertainty in the efficiencies was estimated to be smaller than 5%. The full-energy peak and total efficiencies are listed in Table 2 together with an error of 5%.

Table 2: Simulated full-energy peak efficiencies (FEP) and total efficiencies (TE) corresponding to the gamma rays of ^{24}Na in 50 ml samples of $NaHCO_3$ and NaCl on the HPGe detector.[44]

	Energy (keV)	FEP	TE
$NaHCO_3$	1369	$1.73(9) \times 10^{-2}$	$9.3(5) \times 10^{-2}$
	2754	$9.6(5) \times 10^{-3}$	$8.0(5) \times 10^{-2}$
NaCl	1369	$1.71(9) \times 10^{-2}$	$9.3(5) \times 10^{-2}$
	2754	$9.5(5) \times 10^{-3}$	$8.1(5) \times 10^{-2}$

The coincidence summing correction factors for the efficiencies were obtained by substituting the total efficiencies into Equations 28 and 29. Subsequently, the sum-corrected efficiencies for the $NaHCO_3$ and NaCl samples were calculated by dividing the full-energy peak efficiencies by the determined correction factors. The determined values for the correction factors and sum-corrected efficiencies are listed in Table 3.

Table 3: Correction factors and sum-corrected efficiencies for the gamma rays of ^{24}Na in 50 ml samples of $NaHCO_3$ and NaCl on the HPGe detector.

	Energy (keV)	Correction factor	Sum-corrected ϵ
$NaHCO_3$	1369	1.087(5)	$1.59(8) \times 10^{-2}$
	2754	1.102(6)	$8.7(5) \times 10^{-3}$
NaCl	1369	1.088(5)	$1.57(8) \times 10^{-2}$
	2754	1.103(6)	$8.6(5) \times 10^{-3}$

Furthermore, Monte Carlo simulations were performed by E.R. van der Graaf in [42] to obtain the detection efficiency for the gamma rays emitted by ^{41}Ar in the argon pressure can. In this simulation, the argon container was modeled as a cylinder with a height of 26 cm and a diameter of 7.5 cm. The thickness of the aluminium wall was estimated to be 0.6 mm and the gas density was taken to be 0.02 gcm^{-3}. The efficiencies were simulated for two gamma-ray energies in the decay of ^{41}Ar to ^{41}K namely 1294 and 1677 keV. As mentioned in [44], the relative uncertainty in the efficiencies was estimated to be smaller than 5%. The simulated efficiencies on the HPGe detector for the gamma-ray energies of ^{41}Ar together with a 5% error are listed in Table 4.

Table 4: Simulated efficiencies corresponding to the gamma rays of ^{41}Ar in a 1 l pressure can on the HPGe detector.[42]

Energy (keV)	Efficiency
1294	$3.7(2) \times 10^{-3}$
1677	$3.1(2) \times 10^{-3}$

4.2 Comparison of neutron-activated $NaHCO_3$ and NaCl samples

An overview of the mass and number of Na atoms in the irradiated $NaHCO_3$ and NaCl samples is given in Appendix A.1. The relevant time intervals for the measurement of the $NaHCO_3$ and NaCl sample are shown in Table 5. An error of one minute was taken for the irradiation time and time between irradiation and measurement, since the insertion and removal of the samples from the neutron source were measured to the minute. No error was taken for the measurement time, since it was accurately given by the multichannel analyzer software MAESTRO.

Table 5: Irradiation time (t_{irr}), time between measurement and irradiation (t_{im}), measurement time (t_{meas}) and dead time (δ) for the $NaHCO_3$ and NaCl sample.

	$NaHCO_3$	NaCl
t_{irr}	1.7×10^5 s	4.2×10^5 s
t_{im}	2.3×10^3 s	0.8×10^3 s
t_{meas}	6.2×10^4 s	10.8×10^4 s
δ	0.07%	0.04%

The obtained pulse-height spectra for the NaCl and $NaHCO_3$ sample are shown in Figure 14. In the $NaHCO_3$ and NaCl spectra, eight and six energy peaks (marked in red) can be observed, respectively. The peak corresponding to the lowest energy in both spectra, i.e. the peak on the left, corresponds to an energy of 511 keV. This energy peak results from the detection of annihilation photons in the detector. Moreover, peaks are shown at energies of 1369 and 2754 keV. As stated in subsection 2.3, these gamma-ray peaks are emitted during the decay of the radioactive ^{24}Na to the stable isotope ^{24}Mg. In front of these peaks, the spectrum shows the corresponding Compton edges. In-between the ^{24}Na decay peaks, two smaller peaks are shown corresponding to the single and double escape peak. These escape peaks are the result of the escape of one or both annihilation photons from the detector after a pair-production interaction of the 2754 keV gamma ray. The double and single escape peak have energies of 1732 and 2243 keV, respectively. Furthermore, a relatively small peak is shown with an energy of 4123 keV. This peak is the result of coincidence summing of the full-energy 1369 and 2754 keV gamma rays. The Compton edge shown in front of this sum peak results from the summing of the individual Compton edges.

In addition to these six peaks, the NaCl spectrum shows two more peaks. These correspond to the decay of ^{38}Cl. This isotope is produced by a neutron capture interaction with ^{37}Cl, which is present in NaCl with an abundance of 24.24% and has a capture cross-section of 0.43 barn. During the β-decay of ^{38}Cl, which has a half-life of 37

minutes, to ^{38}Ar, two gamma rays are emitted with branching ratios of 32.9% and 44.0%. These gamma rays have energies of 1643 and 2167 keV, respectively.[2] Due to the relatively low abundance of ^{37}Cl, the relatively low branching ratios of the emitted gamma rays and the short half-life of ^{38}Cl compared to the half-life of ^{24}Na, these peaks are small in comparison with the other peaks observed in the NaCl spectrum.

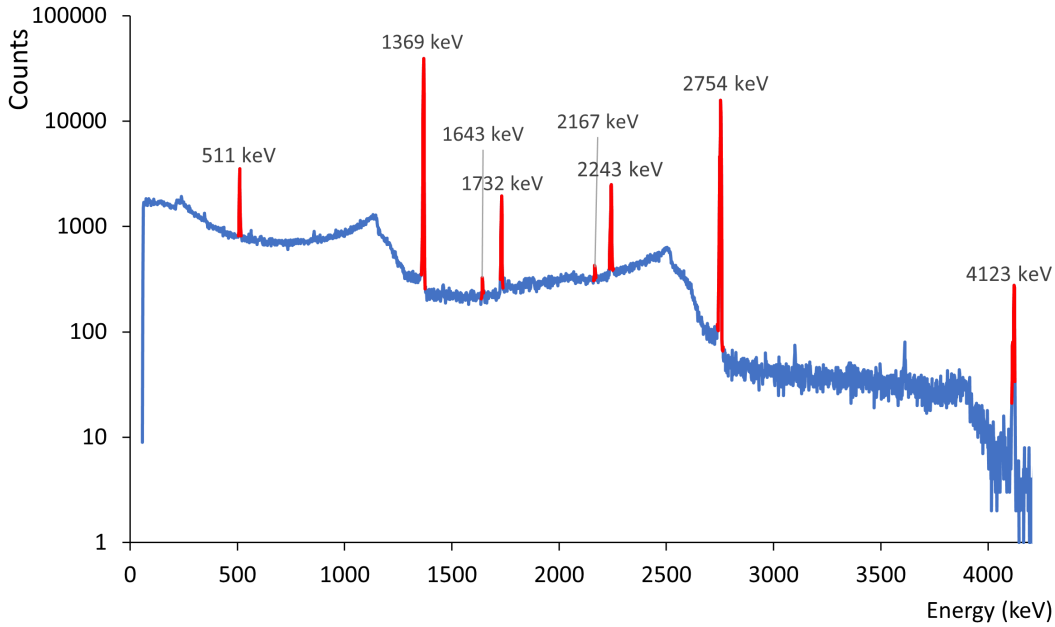

(a) NaCl

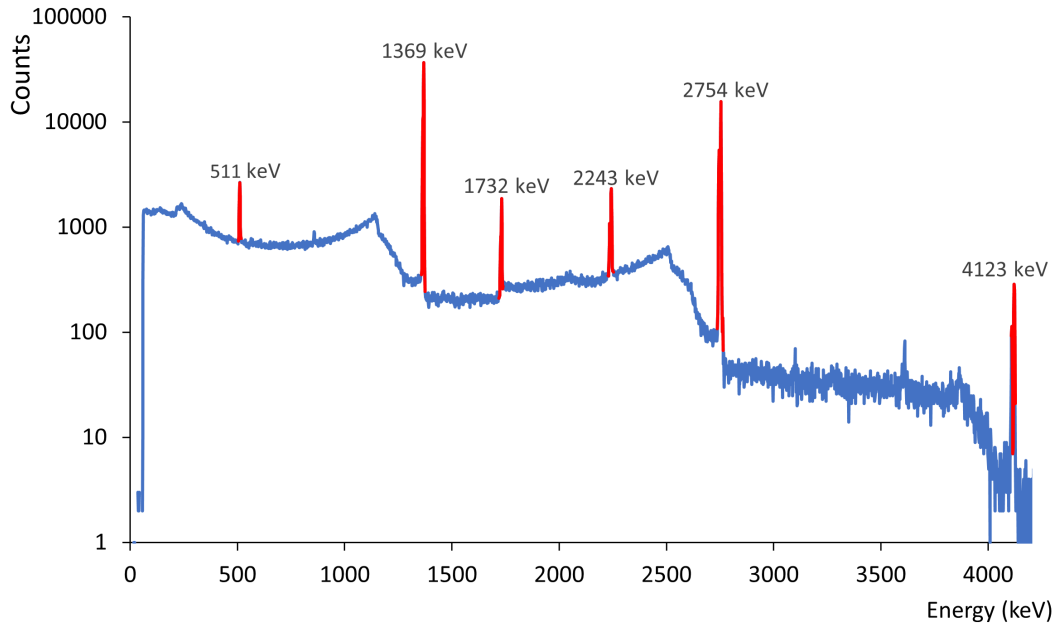

(b) $NaHCO_3$

Figure 14: Obtained pulse-height spectra on a log scale. The peaks are marked in red and indicated by the corresponding gamma-ray energy.

The net area of counts in the 1369, 2754 and 4123 keV peaks were determined from the spectra by subtracting the background from the gross area of counts. A region of interest (ROI) was inserted around the peaks. With the use of the software MAESTRO, the net area corresponding to this ROI was calculated. The uncertainties in the net areas originate from the statistical uncertainties in the determined gross areas and background.

The determined values are shown in Table 6. Combining the time intervals, sum-corrected efficiencies and measured number of counts, as listed in tables 3, 5 and 6, the effective neutron flux incident on the Na atoms in both samples was determined for both the 1369 and 2754 keV peak. These fluxes are also listed in Table 6.

Table 6: Measured net area of counts and correspondingly determined effective neutron flux for the gamma rays of ^{24}Na in the $NaHCO_3$ and NaCl sample.

	Energy peak (keV)	Net area ($\times 10^4$)	Effective Neutron flux ($\times 10^2$ cm^{-2}s^{-1})
$NaHCO_3$	1369	9.69(4)	7.1(4)
	2754	5.35(3)	7.2(4)
	4123	0.116(2)	
NaCl	1369	9.62(5)	2.5(2)
	2754	5.33(3)	2.5(2)
	4123	0.113(4)	

The effective neutron fluxes obtained for the 1369 and 2754 keV energy peaks are in agreement. This is as expected since both gamma rays are emitted from the same radioactive atoms. When comparing the neutron fluxes for the $NaHCO_3$ and NaCl sample, it can be concluded that the calculated effective neutron flux is approximately a factor 2.9 higher for the $NaHCO_3$ sample.

This difference in effective neutron flux is caused by absorption of thermal neutrons within the sample, which leads to a non-uniform flux across the irradiated sample. This self-absorption implies that the neutron flux seen by the Na atoms deeper in the sample is smaller than the flux incident on the outer layer of the sample due to neutron capture by the atoms in the outer layer. In order to quantify this effect, the attenuation coefficients μ were calculated for both the NaCl and $NaHCO_3$ sample with the use of Equation 22. In the calculation, the natural abundance, atomic density and cross-sections corresponding to each isotope in the sample were used. These values are listed in Table 7. The abundance and cross-sections were obtained from the National Nuclear Data Center [2]. The atomic density corresponding to each isotope was calculated using an equation similar to Equation 31 and the volume of the samples, which was approximately 50 ml.

Table 7: Abundance, atomic density and neutron capture cross-section (σ) of the different isotopes in the $NaHCO_3$ and NaCl sample.[2]

	Isotope	Abundance	Atomic density (cm^{-3})	σ (barn)
$NaHCO_3$	^{23}Na	100%	8.6×10^{21}	0.54
	^{1}H	99.99%	8.6×10^{21}	0.33
	^{2}H	0.01%	9.9×10^{17}	5.06×10^{-4}
	^{16}O	99.76%	2.6×10^{22}	1.90×10^{-4}
	^{17}O	0.04%	9.8×10^{18}	3.83×10^{-3}
NaCl	^{23}Na	100%	1.6×10^{22}	0.54
	^{35}Cl	75.76%	1.2×10^{22}	43.63
	^{37}Cl	24.24%	3.8×10^{21}	0.43

The attenuation coefficients μ for $NaHCO_3$ and NaCl were determined to be 0.008 cm^{-1} and 0.532 cm^{-1}, respectively. The attenuation coefficient for NaCl is much larger due to the large neutron capture cross-section of ^{35}Cl. Combining these values for μ with Equation 21, the fraction of the neutron flux after passing a certain thickness of the sample can be calculated. For example, the transmitted fraction of the neutron flux after passing through 1 cm and 2 cm of the NaCl sample are equal to 0.587 and 0.345, respectively. This implies that atoms 2 cm deep into the target only see approximately 35% of the original neutron flux. For the $NaHCO_3$ sample, the fraction corresponding to a thickness of 1 and 2 cm is given by 0.993 and 0.985, respectively. The reduction in flux over the sample is thus negligible. The difference in self-attenuation between the $NaHCO_3$ and NaCl targets is responsible for the factor 2.9 difference in the determined effective neutron flux. For verification, the thermal neutron absorption experiment, as explained in Methods subsection 3.3, was performed.

Since the neutron flux incident on the Na atoms in the measured $NaHCO_3$ sample is almost 3 times higher than the flux seen by the Na atoms in NaCl, $NaHCO_3$ is better for determination of the neutron flux in the indirect measurement of the ^{41}Ar production at the GPTC.

4.3 Thermal neutron absorption

An overview of the mass and number of Na atoms in the irradiated $NaHCO_3$ and NaCl layers is given in Appendix A.2. The relevant time intervals for the irradiation and measurement of the $NaHCO_3$ targets surrounded by a layer of either $NaHCO_3$ or NaCl are shown in Table 8 and 9, respectively.

Table 8: Irradiation time (t_{irr}), time between measurement and irradiation (t_{im}), measurement time (t_{meas}) and dead time (δ) corresponding to the measurement of an irradiated $NaHCO_3$ sample surrounded by an $NaHCO_3$ layer.

	Inner $NaHCO_3$	Outer $NaHCO_3$
t_{irr}	1.8×10^5 s	1.8×10^5 s
t_{im}	6.7×10^3 s	15.8×10^3 s
t_{meas}	8.9×10^3 s	5.4×10^3 s
δ	0.08%	0.07%

Table 9: Irradiation time (t_{irr}), time between measurement and irradiation (t_{im}), measurement time (t_{meas}) and dead time (δ) corresponding to the measurement of an irradiated $NaHCO_3$ sample surrounded by an NaCl layer

	$NaHCO_3$	NaCl
t_{irr}	3.4×10^5 s	3.4×10^5 s
t_{im}	6.4×10^3 s	13.9×10^3 s
t_{meas}	7.2×10^3 s	7.2×10^3 s
δ	0.06%	0.06%

The spectra of both the inner and outer layers consisting of $NaHCO_3$ or NaCl were measured. The obtained net area of counts in the photopeaks are listed in Table 10. Using Equation 18 the corresponding effective neutron fluxes were calculated. These are also presented in the table below.

Table 10: Measured net area of counts and correspondingly determined effective neutron flux for the gamma rays of ^{24}Na in the $NaHCO_3$ and NaCl layers.

	Layer	Energy peak (keV)	Net area ($\times 10^3$)	Effective Neutron flux ($\times 10^2$ cm^{-2}s^{-1})
$NaHCO_3$ in $NaHCO_3$	Inner $NaHCO_3$	1369	18.2(2)	6.2(4)
		2754	9.9(2)	6.2(4)
	Outer $NaHCO_3$	1369	8.7(2)	6.7(4)
		2754	4.9(1)	6.9(4)
$NaHCO_3$ in NaCl	Inner $NaHCO_3$	1369	9.5(3)	3.7(3)
		2754	5.2(2)	3.7(3)
	Outer NaCl	1369	10.4(2)	2.8(2)
		2754	5.7(1)	2.8(2)

The effective neutron fluxes obtained for the inner and outer $NaHCO_3$ layer are almost equal, when taking the uncertainties into account. The inner target seems to be subject to a slightly smaller flux. However, this conclusion is not 100% certain since the uncertainties in the fluxes for the inner and outer layer overlap. A smaller flux of the inner target can be explained by neutron absorption by the outer layer.

In contrast, the $NaHCO_3$ target, which was located inside the NaCl layer, was subject to a larger effective neutron flux than the outer NaCl layer. This was caused by the geometry of the sample. The NaCl layer was only surrounding the $NaHCO_3$ such that there was no NaCl below or on top of the inner target. Therefore, the thermal neutrons reaching the target from above or below were not attenuated by NaCl. However, the thermal neutron flux hitting the sodium atoms in the NaCl layer are attenuated independent of the incoming direction due to self-attenuation. The non-attenuated part of the neutron flux reaching the $NaHCO_3$ target from above and below thus results in the effective neutron flux incident on the inner target being higher than the neutron flux incident on the Na atoms in the outer NaCl layer.

When comparing the effective neutron fluxes of both inner $NaHCO_3$ targets with different outer layers, it can be seen that the determined effective neutron flux for an outer layer of NaCl is 1.7 times smaller than for an outer layer consisting of $NaHCO_3$.

The NaCl layer thus absorbs more thermal neutrons than an $NaHCO_3$ layer of the same dimensions. This is as expected, since the attenuation coefficient of NaCl is much larger than the $NaHCO_3$ coefficient, more specifically 0.532 cm^{-1} with respect to 0.008 cm^{-1}.

4.4 Neutron activation of Argon pressure can

The pulse-height spectrum obtained from the irradiated can filled with argon is shown in Figure 15. The energies and radionuclides corresponding to the peaks have been identified and are shown in the spectrum. The energy peak corresponding to the decay of ^{41}Ar into ^{41}K is marked in red. An analysis of the origin of the other peaks shown in the pulse-height spectrum is given in Appendix B.

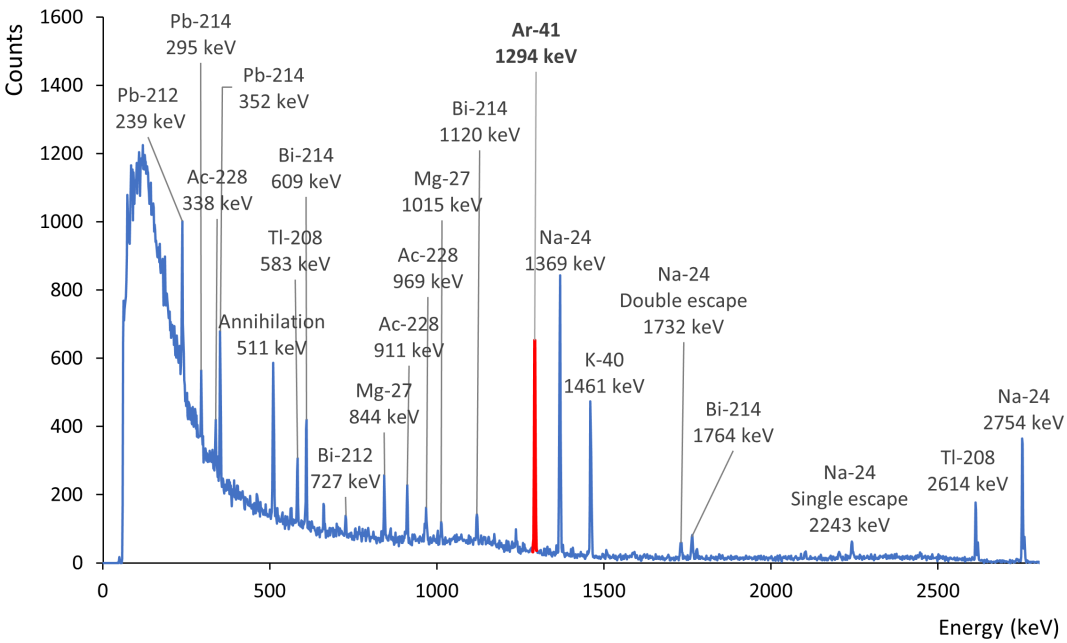

Figure 15: Obtained pulse-height spectrum for the 1 l argon container. The energy peak corresponding to the decay of ^{41}Ar is marked in red. The peaks visible in the spectrum are indicated by the corresponding gamma-ray energy and radioactive isotope. The peaks were identified with the use of the Lund/LBNL Nuclear Data Search[32].

The relevant time intervals for the measurement of the argon bottle are shown in Table 11.

Table 11: Irradiation time (t_{irr}), time between measurement and irradiation (t_{im}), measurement time (t_{meas}) and dead time (δ) corresponding to the irradiation and measurement of the argon container.

t_{irr}	8.2×10^4 s
t_{im}	2.4×10^2 s
t_{meas}	2.0×10^4 s
δ	0.03%

The number of ^{40}Ar atoms present in the bottle was calculated using Equation 33. In this formula, the volume is given by the volume of the pressure can, which is 1 l. f_{Ar} is given by the volume fraction of argon in the Argon 5.0 pressure can (99.999%) multiplied with the natural abundance of ^{40}Ar (99.6%). The number of atoms was found to be $2.95(6) \times 10^{23}$.

In a similar way as for the sodium samples, the net number of counts in the argon peak was determined from the spectrum. It was found to be $1.32(3) \times 10^3$. Using Equation 18 together with the time intervals, the detection efficiency for the 1294 keV gamma ray, as presented in Table 4, and the determined number of ^{40}Ar atoms, the effective neutron flux was determined to be $2.2(4) \times 10^2\,\mathrm{cm}^{-2}\mathrm{s}^{-1}$.

This value is approximately a factor 3.2 smaller than the effective neutron flux incident on the $NaHCO_3$ target. The smaller effective neutron flux incident on the argon gas container is caused by a non-uniform neutron flux in the neutron source. The argon pressure can has a height of 26 cm in comparison with a height of approximately 3 cm for the $NaHCO_3$ target. Since the Am-Be source is positioned below the samples and the neutron flux decreases with distance from the source, the neutron flux seen by the upper part of the argon bottle is smaller than at the bottom. This results in a smaller average effective neutron flux incident on the entire bottle compared to irradiation by a neutron source with a uniform neutron flux. A non-uniform neutron flux thus explains why the effective neutron flux incident on the small $NaHCO_3$ target is larger than the flux incident on the larger argon target.

To make a good comparison between the neutron flux incident on argon and the flux incident on $NaHCO_3$, the neutron flux distribution of the neutron source was determined by measuring the neutron flux at several heights in the neutron source. This was done by stacking multiple containers and placing them inside the neutron source, as mentioned in Methods subsection 3.5. The results of this experiment are stated in the next section.

4.5 Neutron flux distribution

An overview of the mass and number of Na atoms in the irradiated $NaHCO_3$ samples is given in Appendix A.3. The relevant time intervals for the irradiated samples are shown in Table 12 & 13.

Table 12: Irradiation time (t_{irr}), time between measurement and irradiation (t_{im}), measurement time (t_{meas}) and dead time (δ) for the irradiated $NaHCO_3$ samples 2-4.

	Sample 2	Sample 3	Sample 4
t_{irr}	1.6×10^5 s	1.6×10^5 s	1.6×10^5 s
t_{im}	8.6×10^2 s	9.7×10^3 s	1.8×10^4 s
t_{meas}	8.4×10^3 s	7.6×10^3 s	14.4×10^3 s
δ	0.04%	0.03%	0.04%

Table 13: Irradiation time (t_{irr}), time between measurement and irradiation (t_{im}), measurement time (t_{meas}) and dead time (δ) for the irradiated $NaHCO_3$ samples 5-8.

	Sample 5	Sample 6	Sample 7	Sample 8
t_{irr}	1.7×10^5 s	1.7×10^5 s	1.7×10^5 s	1.7×10^5 s
t_{im}	1.7×10^2 s	7.6×10^3 s	1.5×10^4 s	2.0×10^4 s
t_{meas}	7.2×10^3 s	7.0×10^3 s	5.4×10^3 s	7.2×10^3 s
δ	0.02%	0.02%	0.03%	0.05%

In Table 14 the net area of counts and the corresponding uncertainties in the gamma-ray energy peaks of ^{24}Na are listed for the different samples. As before, the effective neutron flux was determined with the use of the net areas of counts, the detection efficiencies, time intervals and Equation 18. The heights of the samples in the neutron source were measured relative to the bottom of the neutron source. The middle of a plastic container was taken as a reference point for each sample. This implies that for sample 8, which was placed at the bottom of the neutron source, the relative height is equal to one half the height of a single plastic container, i.e. 1.93 cm. The height differences between successive samples was one container, since they were stacked on top of each other. This yields the relative heights as listed in Table 14.

Table 14: Measured net area of counts and correspondingly determined effective neutron flux for the gamma rays of ^{24}Na in the $NaHCO_3$ samples. The relative heights of the samples are also listed.

	Relative height (cm)	Energy peak (keV)	Net area ($\times 10^3$)	Effective Neutron flux ($\times 10^2$ cm^{-2}s^{-1})
Sample 8	1.9	1369	8.1(1)	4.7(3)
		2754	4.5(1)	4.8(3)
Sample 4	5.8	1369	11.6(2)	3.5(2)
		2754	6.1(1)	3.4(2)
Sample 7	9.6	1369	3.2(1)	2.3(2)
		2754	1.69(5)	2.2(2)
Sample 3	13.5	1369	3.7(1)	1.8(2)
		2754	2.00(6)	1.8(2)
Sample 6	17.3	1369	2.9(1)	1.5(1)
		2754	1.53(5)	1.43(9)
Sample 2	21.2	1369	3.6(2)	1.5(2)
		2754	1.9(1)	1.4(2)
Sample 5	25.0	1369	2.2(1)	1.00(7)
		2754	1.23(5)	1.02(7)

The effective neutron fluxes obtained from the number of counts in the 1369 keV peak were plotted as a function of height. This plot is shown in Figure 16. A linear interpolation was performed on the data.

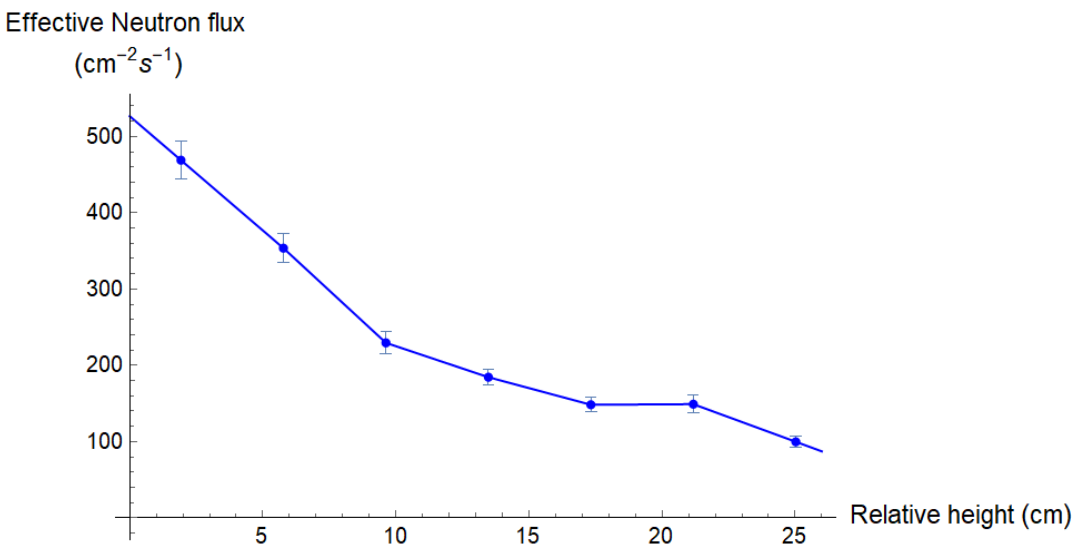

Figure 16: A linear interpolation of the effective neutron fluxes obtained from the data corresponding to the 1369 keV peak is shown as a function of height.

From this graph it can be concluded that the effective neutron flux decreases as a function of height and the neutron flux is thus not uniform over the height of a target. To determine the average effective neutron flux incident on an $NaHCO_3$ target with similar dimensions as the argon bottle, the graph had to be extrapolated to heights below 1.9 cm and above 25.0 cm, since the height of the argon bottle equals 26 cm.

The curve, shown in Figure 16, was integrated over a height of 26 cm and subsequently divided by this same height. This yielded an average effective neutron flux of 240 $cm^{-2}s^{-1}$. An upper and lower bound for the average neutron flux were determined by drawing curves through the top and bottom of the error bars corresponding to each data point, respectively. As before, these curves were integrated over a height of 26 cm and subsequently divided by this same height. The upper and lower bound were found to be 254 and 226 $cm^{-2}s^{-1}$, respectively. This resulted in an average effective neutron flux of $2.4(2) \times 10^2$ $cm^{-2}s^{-1}$. A similar plot and calculation was performed for the neutron fluxes obtained with the data from the 2754 keV energy peaks. This also yielded an average neutron flux of $2.4(2) \times 10^2$ $cm^{-2}s^{-1}$ for the inter- and extrapolated curve. Therefore, the average effective neutron flux incident on $NaHCO_3$ over a height of 26 cm was concluded to be $2.4(2) \times 10^2$ $cm^{-2}s^{-1}$.

The obtained values for the average effective neutron flux might be slightly off, since the curve obtained by linear interpolation and extrapolation does not represent the relation between neutron flux and height exactly. Furthermore, the determined neutron fluxes do not correspond to a single height in the neutron source as was assumed in the calculations. Instead, these fluxes are an average over the height of a single plastic container with a size of 3.85 cm resulting in an uncertainty in the assumed relative heights of the samples.

As stated in Results subsection 4.4, the effective neutron flux determined from the irradiated argon bottle was found to be $2.2(4) \times 10^2$ $cm^{-2}s^{-1}$. This value is in agreement with the value of $2.4(2) \times 10^2$ $cm^{-2}s^{-1}$ obtained from the irradiated $NaHCO_3$ stacks, when taking the uncertainties into account. This implies that the effective neutron fluxes incident on an $NaHCO_3$ sample or incident on an argon sample with the same geometry are approximately equal. Therefore, it can be concluded that the neutron activation of $NaHCO_3$ for determination of the thermal neutron flux can be used as an indirect measurement technique for estimating the production of ^{41}Ar.

General discussion point

Part of the pulse-height spectra, obtained in the earlier described experiments, showed abnormal peaks. In front of the regular photopeaks, smaller peaks were detected. An example of such a 'double' peak is shown in Figure 17.

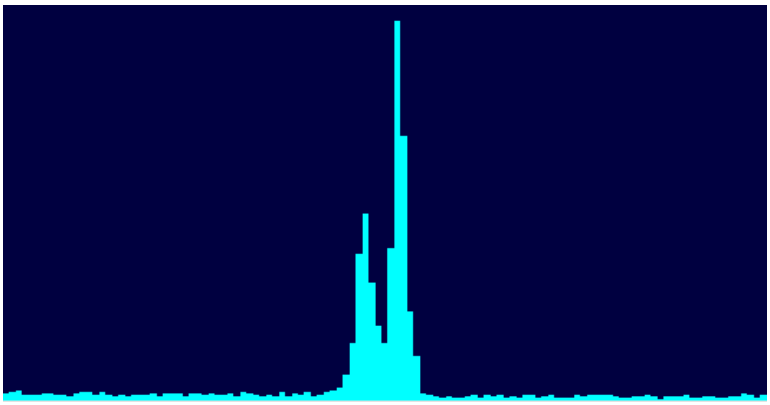

Figure 17: Part of a spectrum showing a smaller peak right in front of the actual photopeak.

To determine the origin of the counts in this smaller peak, a similar pulse-height spectrum was obtained with the use of a different multichannel analyzer showing only the regular photopeaks. The total number of counts in a photopeak and the corresponding smaller peak in front were determined for the abnormal spectrum. These were compared with the number of counts in the photopeak corresponding to the regular spectrum. These turned out to be approximately equal. Therefore, it can be concluded that the small peak contains pulses which are supposed to be in the photopeak. The pulses in the entire double peak, including the smaller peak, were thus taken into account for determination of the photopeak content. This abnormal behaviour of the spectrum is expected to be caused by some error in the multichannel analyzer equipment.

4.6 $NaHCO_3$ irradiation at GPTC

Calibration second HPGe detector

The relevant time intervals for the measurement of the $NaHCO_3$ sample on the first and second HPGe detector are listed in Table 15.

Table 15: Time between measurement and irradiation (t_{im}), measurement time (t_{meas}) and dead time (δ) corresponding to the measurement of an $NaHCO_3$ sample on the two HPGe detectors.

	HPGe detector 1	HPGe detector 2
t_{im}	9.2×10^3 s	1.1×10^3 s
t_{meas}	7.2×10^3 s	7.2×10^3 s
δ	0.09%	0.41%

Using these time intervals, the determined net area of counts in the photopeaks of both detectors, the efficiencies of the first detector, as listed in Table 3, and Equation 39, the efficiencies of the second HPGe detector were determined. The obtained values are shown in Table 16 together with the determined number of counts in the photopeaks corresponding to the decay of ^{24}Na and the efficiencies of the first detector.

Table 16: Net area of counts and sum-corrected efficiencies for the gamma rays of ^{24}Na in a 50 ml sample of $NaHCO_3$ for HPGe detector 1 (ϵ_1) and HPGe detector 2 (ϵ_2).

	HPGe detector 1		HPGe detector 2	
Energy peak (keV)	Net area ($\times 10^3$)	ϵ_1	Net area ($\times 10^3$)	ϵ_2
1369	15.6(2)	$1.59(8) \times 10^{-2}$	16.8(2)	$1.55(9) \times 10^{-2}$
2754	8.9(2)	$8.7(5) \times 10^{-3}$	9.1(2)	$8.0(5) \times 10^{-3}$

Results irradiation at GPTC

During the measurement at the GPTC, the $NaHCO_3$ samples were exposed to 33 irradiations. The first irradiation took place at 07:15 in the morning. The time intervals between the first irradiation and the remaining irradiations are listed in Table A.5 in Appendix A.4. Table A.5 also shows the relative neutron flux corresponding to each irradiation. Each irradiation was assumed to last one minute. This is not entirely correct. However, since the irradiation time is much smaller than the half-life of ^{24}Na (15 hours), an error in the irradiation time of the order of minutes does not significantly effect the eventually determined effective neutron flux.

The relevant time intervals for the measurement of the $NaHCO_3$ samples at the PARTREC facility are presented in Table 17. Moreover, the net number of counts in the 1369 keV peak corresponding to the decay of ^{24}Na is listed for each sample. These were determined from the obtained pulse-height spectra.

The effective neutron fluxes, also presented in Table 17, were calculated with the use of Equation 19. This formula makes use of the efficiencies of HPGe detectors 1 and 2 and the number of ^{23}Na atoms in each sample, which are presented in Table 16 and A.4, respectively. The time intervals between end of irradiation and start/end of measurement were determined for each irradiation and sample separately. They were determined using the known time of the first irradiation, the time between the first irradiation and the measurement and the time intervals between the first irradiation and the other irradiations, as listed in Table A.5.

Table 17: The time between measurement and first irradiation ($t_{im,1}$), measurement time (t_{meas}) and dead time (δ) corresponding to the measurement of the $NaHCO_3$ samples irradiated at the GPTC are listed. The net area of counts in the 1369 keV peak of ^{24}Na with the correspondingly determined effective neutron flux are also stated for each sample.

	$t_{im,1}$ ($\times 10^4$ s)	t_{meas} ($\times 10^3$ s)	δ	Net area ($\times 10^3$)	Effective Neutron flux ($\times 10^6$ cm^{-2}s^{-1})
Sample 1	6.8	53.5	0.05%	No peak visible	-
Sample 2	5.6	1.8	0.05%	No peak visible	-
Sample 3	5.7	1.8	0.01%	No peak visible	-
Sample 4	5.6	0.3	1.98%	13.0(2)	23(8)
Sample 5	5.7	0.3	0.39%	3.04(7)	5(2)
Sample 6	5.8	9.3	0.07%	0.98(5)	0.056(5)
Sample 7	6.6	54.0	0.01%	0.50(8)	0.007(2)
Sample 8	5.9	0.7	0.18%	3.22(7)	2.2(3)

The concentration of ^{40}Ar atoms in the air was calculated using Equation 33, where the pressure was taken to be atmospheric pressure (101 325 Pa) and the temperature was taken to be room temperature (293(5) K). The fraction of ^{40}Ar molecules in the air is given by the natural abundance of ^{40}Ar in argon multiplied with the volume fraction of argon in air. The ^{40}Ar concentration in air was found to be $2.32(4) \times 10^{23}$ atoms m^{-3}.

Substituting this concentration, the obtained effective neutron fluxes, an irradiation time of 60 seconds, the neutron capture cross-section and the decay constant of ^{41}Ar into Equation 11, yields the produced activity of ^{41}Ar per m^3 by thermal neutron activation. The produced ^{41}Ar activities are listed in Table 18 for the measurements corresponding to $NaHCO_3$ samples 4 to 8.

Table 18: Produced ^{41}Ar activity concentrations calculated from the measurements of $NaHCO_3$ samples 4 to 8.

	Activity concentration ^{41}Ar ($\times 10^3$ Bq m^{-3})
Sample 4	23(8)
Sample 5	5(2)
Sample 6	0.055(9)
Sample 7	0.007(2)
Sample 8	2.1(4)

The highest activity of ^{41}Ar is produced at the location of $NaHCO_3$ sample 4, i.e. close to the energy degrader. The next highest activities correspond to samples 5 and 8. These were both placed close to the energy selection system (ESS). Samples 6 and 7 were subject to the smallest effective neutron fluxes and as a result the least amount of ^{41}Ar was produced at the corresponding locations further along the beam line. Therefore, it can be concluded that the largest effective neutron flux, and thus the largest ^{41}Ar production, takes place near beam-modifying devices like the energy degrader and energy selection system. When one gets further away from these beam-modifying

devices, the neutron flux decreases with several orders of magnitude.

One would expect a homogeneous distribution of thermal neutrons throughout the cyclotron bunker due to the large mean free path of thermal neutrons in air. Taking into account the most abundant isotopes in air, the mean free path of thermal neutrons can be calculated using Equation 4 and the values stated in Table 19. This gives a mean free path of 2.7×10^3 cm implying that the thermal neutrons spread throughout the cyclotron bunker.

Table 19: Abundance, atomic density and total cross-section (σ_{tot}) at thermal energies (0.025 eV) of the most abundant isotopes in air. The atomic densities at room temperature and atmospheric pressure were calculated using Equation 33. The abundances and total cross-sections were retrieved from [1, 2, 45–47].

Isotope	Abundance	Atomic density (cm^{-3})	σ_{tot} (barn)
^{14}N	77.79%	1.9×10^{19}	12.19
^{16}O	20.90%	5.2×10^{18}	3.92
^{40}Ar	0.93%	2.3×10^{17}	1.32

The variation in neutron flux throughout the cyclotron bunker can be explained by the fact that ^{23}Na does not only capture thermal neutrons. As can be seen from the plot of neutron capture cross-section versus neutron energy for ^{23}Na, as shown in Figure 18, higher-energy neutrons can also be captured.

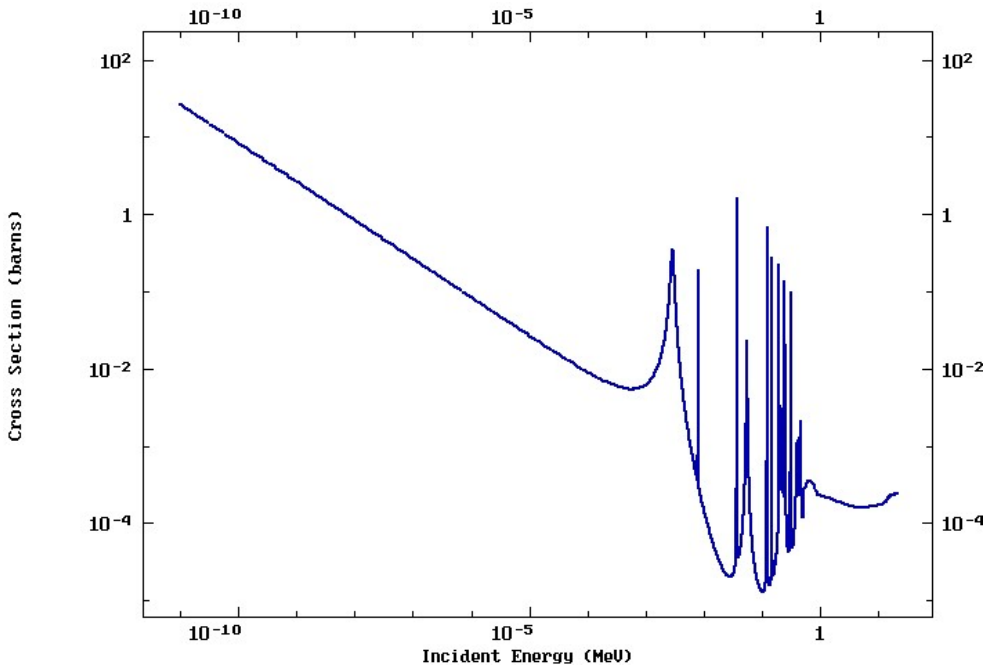

Figure 18: Neutron capture cross-section as a function of neutron energy corresponding to ^{23}Na.[48]

Since neutrons are produced when protons lose energy through interactions with beam-modifying devices, more neutrons are present close to these devices. Therefore, more higher-energy neutrons are captured near these devices resulting in higher effective

neutron fluxes close to beam-modifying devices with respect to fluxes measured at locations further away.

The observation that, besides thermal neutrons, also higher-energy neutrons are captured by ^{23}Na does not significantly influence the obtained results for the produced ^{41}Ar concentrations since the neutron capture cross-sections for ^{40}Ar and ^{23}Na show similar behaviours for neutrons with higher energies. This can be seen when comparing Figure 19, which shows the neutron capture cross-section as a function of neutron energy for ^{40}Ar, with Figure 18. Therefore, the obtained values for the produced ^{41}Ar activity still represent the amount of ^{41}Ar produced in the cyclotron bunker. However, the activity is not entirely produced by thermal neutron capture, but also by the capture of higher-energy neutrons.

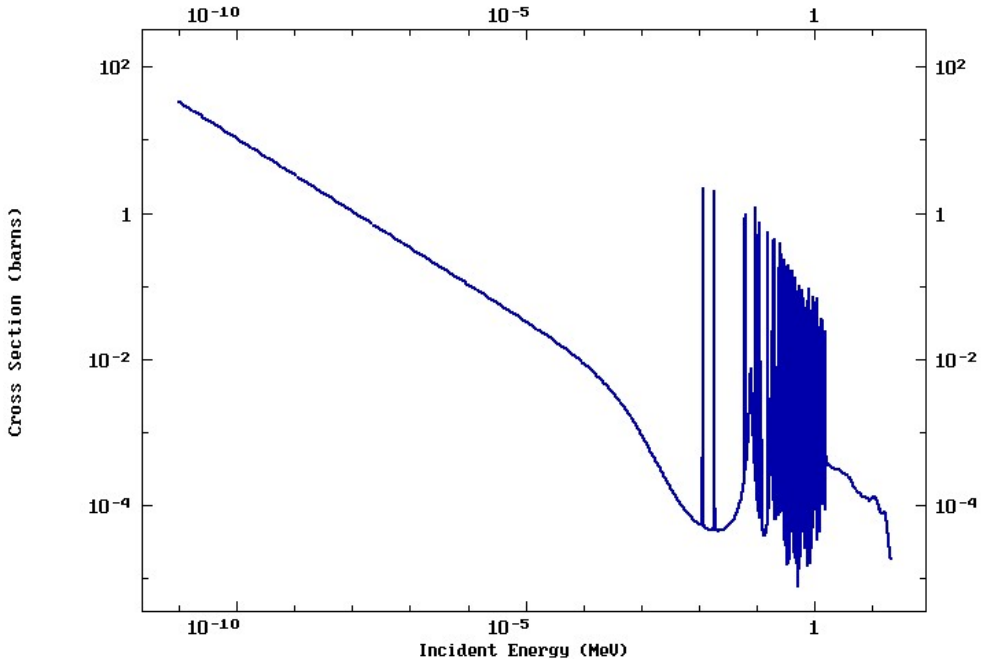

Figure 19: Neutron capture cross-section as a function of neutron energy corresponding to ^{40}Ar.[49]

For samples 1 to 3, which were located respectively in the treatment room and near the entrance maze of the cyclotron bunker, no peak could be distinguished at 1369 keV in the obtained pulse-height spectra. This implies that the activity induced in these $NaHCO_3$ samples by thermal neutron irradiation was lower than the detection limit. To obtain an indication of the maximum amount of ^{41}Ar produced at these locations, an upper limit was determined. The effective neutron flux and ^{41}Ar production corresponding to the detection of a single count in the 1369 keV energy peak were calculated. This yielded the values for the upper limits listed in Table 20. The difference in the values for the upper limits is caused by the difference in measurement time of the samples on the HPGe detectors.

Table 20: Upper limits for the effective neutron flux and produced ^{41}Ar activity concentration calculated from the measurement of $NaHCO_3$ samples 1 to 3.

	Upper limit for Effective Neutron flux ($cm^{-2}s^{-1}$)	Upper limit for Activity concentration ^{41}Ar ($Bq\ m^{-3}$)
Sample 1	14	0.014
Sample 2	2.7×10^2	0.27
Sample 3	2.7×10^2	0.26

From these upper limits, it can be concluded that the ^{41}Ar activity induced in the treatment room and the entrance maze is small. The low thermal neutron flux in the entrance maze is the result of good shielding by the walls of the maze. The ^{41}Ar production in the treatment room is low because the protons already have much lower energies and the proton beam current is significantly reduced once entering the treatment room resulting in less neutron production.

In the Netherlands, facilities such as universities, hospitals and industry need a licence to be allowed to discharge radioactivity into surface water, sewage systems and air. Licence holders need to demonstrate that the amount of discharged radioactivity does not exceed the limits. For the medical sector, a discharge limit exists for the licensed discharge of ^{41}Ar into the air.[50] In the case of the Groningen Proton Therapy Center, the limit for the discharge of ^{41}Ar is 8 GBq per year[51].

To establish whether the amount of ^{41}Ar activity discharged from the GPTC exceeds the discharge limit, the total activity of ^{41}Ar produced and discharged from the cyclotron bunker into the air was determined. Since the amount of ^{41}Ar produced in the treatment room and entrance maze is small, the total activity discharged from these locations into the air has only a very small contribution to the total amount of ^{41}Ar activity discharged. Therefore, this contribution was not taken into account.

An upper bound for the total produced ^{41}Ar activity in the cyclotron bunker was calculated from the produced activity concentrations and the size of the cyclotron bunker. The size of the cyclotron bunker was estimated from the floor map of the GPTC. This floor map, zoomed in on the cyclotron bunker, is shown in Figure 20.

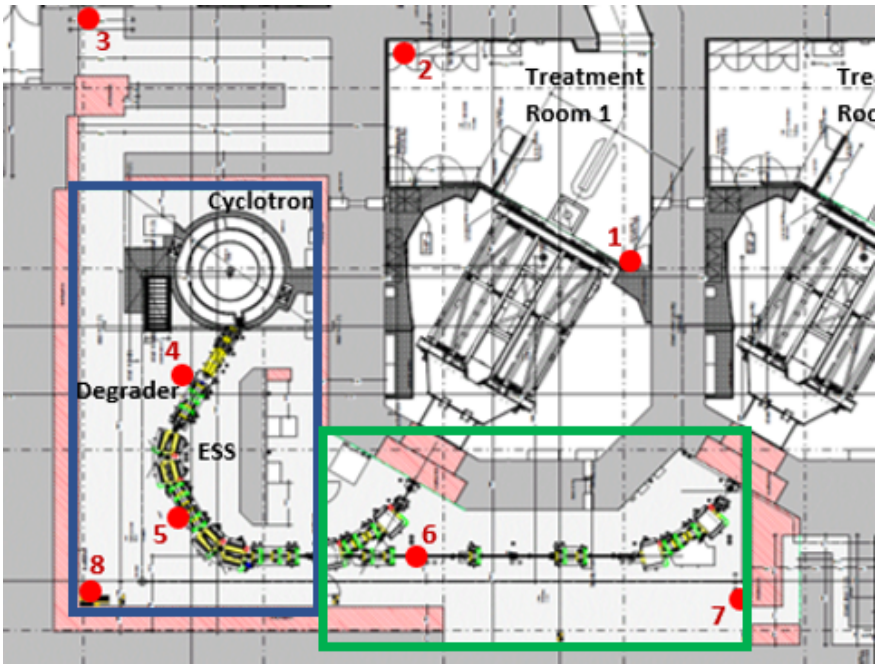

Figure 20: Floor map of the Groningen Proton Therapy Center (GPTC) zoomed in on the cyclotron bunker. Original floor map was retrieved from Marc-Jan van Goethem. The cyclotron bunker is divided into two parts. The left part, framed in blue, contains the cyclotron, energy degrader and energy selection system. The continuation of the beam line is situated in the right region of the bunker, which is framed in green.

Because of the large difference in produced activity concentrations between the samples located near the degrader and ESS, and the samples placed further along the beam line, the total activity was calculated for two parts of the cyclotron bunker separately.

The left part of the cyclotron bunker, indicated with the blue frame, was roughly estimated to have an area of $10 \times 17\,\mathrm{m}$. The area of the right part of the bunker, indicated with the green frame, was estimated to be $7 \times 17\,\mathrm{m}$. A height of $4\,\mathrm{m}$ was taken. These broad estimates led to volumes of 680 and $476\,\mathrm{m}^3$ for the left and right region of the bunker, respectively.

To obtain an upper bound for the total activity of ^{41}Ar produced around the cyclotron, degrader and ESS, the ^{41}Ar activity concentration calculated from $NaHCO_3$ sample 4 was multiplied with the determined volume of $680\,\mathrm{m}^3$. For the total produced activity further along the beam line, the volume corresponding to the right part of the bunker was multiplied with the activity concentration of sample 6. The ^{41}Ar activities for samples 4 and 6 were used since these correspond to the largest local production of ^{41}Ar. Therefore, using these values results in an upper limit for the total produced activity in the two regions. These calculations yielded total activities of 1.6×10^7 and $2.6 \times 10^4\,\mathrm{Bq}$, respectively. These values add up to a total ^{41}Ar activity of $1.6 \times 10^7\,\mathrm{Bq}$ in the entire cyclotron bunker. Multiplying this ^{41}Ar activity with the number of treatment days per year, which is equal to 261 days, yields a yearly emission of ^{41}Ar equal to $4\,\mathrm{GBq}$, assuming all of the produced ^{41}Ar activity is emitted into the atmosphere.

However, not all of the produced ^{41}Ar activity is discharged through the ventilation system. At the GPTC, a volume of air equal to the volume of the cyclotron bunker is emitted through the ventilation system every hour [51]. This implies that 68% of the ^{41}Ar produced will be expelled from the cyclotron bunker, while the remaining 32% decays inside the bunker. From the 1.6×10^7 Bq produced in the cyclotron bunker during a full day of patient irradiations, 1.1×10^7 Bq is thus expelled into the atmosphere. This results in a yearly emission of ^{41}Ar equal to 3 GBq. It can be concluded that this amount of ^{41}Ar activity discharged from the cyclotron bunker, i.e. 3 GBq per year, is well below the discharge limit for the GPTC of 8 GBq per year.

5 Conclusion

In this study the amount of ^{41}Ar production at the Groningen Proton Therapy Center (GPTC) was estimated using an indirect measurement technique. Instead of activating pure argon, Na atoms contained in $NaHCO_3$ targets were neutron-activated at the GPTC. From the activated Na atoms the incident effective neutron flux was obtained. This was combined with the thermal neutron capture cross-section of ^{40}Ar to obtain an estimation of the ^{41}Ar production.

Initially, an experiment was performed to determine whether $NaHCO_3$ or NaCl would be a better sodium-containing substance for measuring the incident neutron flux. Both an $NaHCO_3$ sample and an NaCl sample were neutron-activated with the use of the Am-Be neutron source at the Particle Therapy Research Center (PARTREC). After irradiation, the gamma-ray spectra emitted by the samples were measured. The number of gamma rays detected in the peaks corresponding to the decay of ^{24}Na were determined in order to calculate the effective neutron flux incident on both samples. The fluxes were determined to be $7.1(4) \times 10^2$ and $2.5(2) \times 10^2\,\mathrm{cm^{-2}s^{-1}}$ for the $NaHCO_3$ and NaCl sample, respectively. The effective neutron flux seen by the Na atoms in NaCl was smaller, because of the significant thermal neutron absorption by chlorine in NaCl. Therefore, $NaHCO_3$ samples were used for determining the thermal neutron flux at the GPTC.

Afterwards, a gas container filled with almost pure argon was irradiated by the same neutron source. The pulse-height spectrum emitted by the bottle was measured and the number of gamma rays in the peak corresponding to the decay of ^{41}Ar was determined. Using this, the neutron flux incident on the ^{40}Ar atoms in the gas container was calculated to be $2.2(4) \times 10^2\,\mathrm{cm^{-2}s^{-1}}$. This value was a factor 3.2 smaller than the effective neutron flux incident on the $NaHCO_3$ sample due to the non-uniform neutron flux distribution inside the neutron source. To obtain a good comparison between the effective neutron fluxes incident on $NaHCO_3$ and argon, the neutron flux distribution over the height of the neutron source was studied. Taking the obtained neutron flux distribution into account yielded an effective neutron flux of $2.4(2) \times 10^2\,\mathrm{cm^{-2}s^{-1}}$ for an $NaHCO_3$ target with a height equal to the height of the argon gas container. This value is in agreement with the incident neutron flux for argon. An argon and $NaHCO_3$ target are thus subject to the same effective thermal neutron flux. Therefore, $NaHCO_3$ can be used for the indirect measurement of ^{41}Ar production.

Finally, eight $NaHCO_3$ samples were placed throughout the cyclotron bunker and treatment room of the GPTC for the indirect measurement of the ^{41}Ar production. After a full day of patient irradiations, the neutron-activated samples were transported to the PARTREC facility for measurement of the emitted gamma-ray spectra. From the spectra, the effective neutron flux incident on each target as well as the corresponding produced activity concentration of ^{41}Ar were calculated. No effective neutron flux could be determined for the samples located in the treatment room and near the entrance maze of the cyclotron bunker. Therefore, an upper limit for the produced ^{41}Ar activity of about $0.3\,\mathrm{Bqm^{-3}}$ was calculated for these locations. The calculations for the remaining $NaHCO_3$ samples yielded activity concentrations ranging from $0.007(2) \times 10^3\,\mathrm{Bqm^{-3}}$

near the exit maze of the cyclotron bunker up to $23(8) \times 10^3\,\mathrm{Bqm^{-3}}$ close to the energy degrader. From these activity concentrations, the size of the bunker and the ventilation rate, the total ^{41}Ar activity discharged from the bunker was found to be 3 GBq per year. This amount of discharged ^{41}Ar activity by the GPTC is well below the licensed discharge limit of 8 GBq per year.

References

[1] *Air: its composition and properties*, http://www.uigi.com/air.html (visited on 05/25/2021).

[2] National Nuclear Data Center, *Nudat 2.8*, https://www.nndc.bnl.gov/nudat2/reCenter.jsp?z=11&n=13 (visited on 04/21/2021).

[3] J. H. Chao, W. S. Liu, and C. Y. Chen, "Estimation of Argon-41 concentrations in the vicinity of a high-energy medical accelerator", Radiation Measurements **42**, 1538–1544 (2007).

[4] A. H. Sullivan, "Radioactivity induced in high energy particle accelerators", in *A guide to radiation and radioactivity levels near high energy particle accelerators* (Nuclear Technology Publishing, Ashford, Kent, England, 1992) Chap. 4.

[5] *Particle Therapy Research Center – PARTREC*, https://umcgresearch.org/-/partrec (visited on 06/23/2021).

[6] H. Cember and T. E. Johnson, "Interaction of radiation with matter", in *Introduction to health physics*, 4th ed. (McGraw-Hill, USA, 2009) Chap. 5.

[7] J. E. Turner, "Neutrons, fission, and criticality", in *Atoms, radiation, and radiation protection*, 3rd ed. (WILEY-VCH Verlag GmbH & Co. KGaA, Weinheim, DE, 2007) Chap. 9.

[8] G. F. Knoll, *Radiation detection and measurement*, 4th ed. (John Wiley & Sons, Inc., USA, 2010).

[9] W. N. Cottingham and D. A. Greenwood, *An introduction to nuclear physics* (Cambridge University Press, Cambridge, UK, 2001).

[10] S. R. Cherry, J. A. Sorenson, and M. E. Phelps, *Physics in nuclear medicine* (Saunders Elsevier, Philadelphia, PA, USA, 2012).

[11] S. N. Ahmed, "Interaction of radiation with matter", in *Physics and engineering of radiation detection*, 1st ed. (Academic Press, Amsterdam, NL, 2007) Chap. 2.

[12] W. D. Newhauser and R. Zhang, "The physics of proton therapy", Physics in Medicine & Biology **60**, R155–R209 (2015).

[13] A. Pérez-Andújar et al., "Neutron production from beam-modifying devices in a modern double scattering proton therapy beam delivery system", Physics in Medicine & Biology **54**, 993–1008 (2009).

[14] *Neutron capture*, https://www.radioactivity.eu.com/site/pages/Neutrons_Capture.htm (visited on 04/23/2021).

[15] H. Vainionpää, M. Paaso, and P. Salmi, *Brief description of neutron technologies*, https://neutrongate.com/theory/ (visited on 04/27/2021).

[16] Budapest Neutron Centre, *The radiative neutron capture process*, https://www.bnc.hu/?q=radiative_neutron_capture (visited on 04/27/2021).

[17] S. Brandenburg, "Thermal neutron flux determination through ^{24}Na-production in NaI", unpublished, 2021.

[18] NIST, *Fundamental physical constants*, (2019) https://physics.nist.gov/cuu/Constants/index.html (visited on 05/30/2021).

[19] R. B. Firestone, Z. Revay, and T. Belgya, "Thermal neutron capture cross sections and neutron separation energies for ^{23}Na(n,γ)", Physical Review C **89**, 014617 (2014).

[20] R. B. Firestone, "Nuclear Data Sheets for A = 24", Nuclear Data Sheets **108**, 2319–2392 (2007).

[21] V. Fischer, L. Pagani, L. Pickard, A. Couture, S. Gardiner, C. Grant, J. He, T. Johnson, E. Pantic, C. Prokop, R. Svoboda, J. Ullmann, and J. Wang, "Measurement of the neutron capture cross section on argon", PHYSICAL REVIEW D **99**, 103021 (2019).

[22] J. C. Morrison, "Charge carriers in semiconductors", in *Modern physics for scientists and engineers*, 2nd ed. (Academic Press, USA, 2015) Chap. 9.

[23] *Semiconductor detectors*, https://www.nuclear-power.net/nuclear-engineering/radiation-detection/semiconductor-detectors/ (visited on 05/25/2021).

[24] N. Connor, *What is germanium detector – principle of operation – definition*, (2019) https://www.radiation-dosimetry.org/what-is-germanium-detector-principle-of-operation-definition/ (visited on 05/25/2021).

[25] N. Connor, *What is high purity germanium detector – hpge – definition*, (2019) https://www.radiation-dosimetry.org/what-is-high-purity-germanium-detector-hpge-definition/ (visited on 05/25/2021).

[26] *High-resolution gamma-ray spectroscopy with hpge detectors*, https://www.mirion.com/learning-center/lab-experiments/high-resolution-gamma-ray-spectroscopy-with-hpge-detectors-lab-experiments (visited on 05/25/2021).

[27] P. Hofmann, *Solid state lectures (lecture 7)*, https://philiphofmann.net/solid-state-physics-book/solid-state-lectures/ (visited on 02/04/2021).

[28] *Natural radioactivity*, https://www.radioactivity.eu.com/site/pages/Natural_Radioactivity.htm (visited on 05/07/2021).

[29] Rijksinstituut voor Volksgezondheid en Milieu, *Straling van natuurlijke oorsprong*, https://www.rivm.nl/straling-en-radioactiviteit/straling-van-natuurlijke-oorsprong (visited on 05/07/2021).

[30] USGS, *Thorium*, https://pubs.usgs.gov/of/2004/1050/PalosVerdesRn.htm#thorium.htm (visited on 05/25/2021).

[31] USGS, *Uranium*, https://pubs.usgs.gov/of/2004/1050/uranium.htm (visited on 05/25/2021).

[32] S. Y. F. Chu, L. P. Ekström, and R. B. Firestone, *The Lund/LBNL Nuclear Data Search*, (1999) http://nucleardata.nuclear.lu.se/toi/index.asp (visited on 05/07/2021).

[33] K. Debertin and R. G. Helmer, "Efficiency calibration and emission-rate measurements", in *Gamma and x-ray spectrometry with semiconductor detectors* (North-Holland, Amsterdam, NL, 1988) Chap. 4.

[34] *Personal communication with Peter Dendooven.*

[35] A. Didi, A. Dadouch, J. Tajmouati, A. Maghnouj, M. Benchiekh, and O. Jai, "New design of thermal neutron flux distribution of Am–Be neutron source irradiation in paraffin moderator using MCNP-6", Moroccan Journal of Chemistry **4**, 285–288 (2016).

[36] T. E. Johnson and B. K. Birky, "Neutron production, shielding and activation", in *Health physics and radiological health*, 4th ed. (Wolters Kluwer, CN, 2011) Chap. 7.

[37] NIST, *Basic atomic spectroscopic data*, (2013) https://physics.nist.gov/PhysRefData/Handbook/periodictable.htm (visited on 05/30/2021).

[38] Messer Group GmbH, *Cangas, the "smaller" alternative*, https://elmemesser.lv/wp-content/uploads/2020/04/1875798247c1e7e4a6531c1fbb10d043_compressed.pdf (visited on 05/24/2021).

[39] S. J. Blundell and K. M. Blundell, "Introduction", in *Concepts in thermal physics*, 2nd ed. (Oxford University Press, GB, 2010) Chap. 1.

[40] R. K. Smither and L. R. Greenwood, "Measurement of the ^{27}Al(n,2n)^{26}Al reaction cross section for fusion reactor applications", Journal of Nuclear Materials **123**, 1071–1077 (1984).

[41] S. Padalino, H. Oliver, and J. Nyquist, *Aluminum activation*, https://www.geneseo.edu/nuclear/aluminum-activation-results (visited on 05/26/2021).

[42] E. R. van der Graaf, "HPGe detector simulations efficiencies for ^{41}Ar in a bottle", unpublished, 2021.

[43] D. Yeung and J. Palta, "Proton Therapy", in *Encyclopedia of radiation oncology* (Springer, Berlin, Heidelberg, 2013).

[44] E. R. van der Graaf, "HPGe detector simulations efficiencies ^{24}Na in NaCl and NaHCO3 in a 50 ml pill box", unpublished, 2021.

[45] T. Kawano, (2012) https://www-nds.iaea.org/exfor/servlet/E4sGetTabSect?SectID=8948917&req=46&PenSectID=13595129 (visited on 06/26/2021).

[46] M. B. Chadwick and P. G. Young, (2011) https://www-nds.iaea.org/exfor/servlet/E4sGetTabSect?SectID=8943550&req=71&PenSectID=13590855 (visited on 06/26/2021).

[47] Hale, Paris, Young, and Chadwick, (2018) https://www.nndc.bnl.gov/exfor/servlet/E4sGetTabSect?SectID=383181&req=32491&PenSectID=333978 (visited on 06/26/2021).

[48] D. C. Larson, (2011) https://www.nndc.bnl.gov/exfor/servlet/E4sMakeE4 (visited on 06/26/2021).

[49] T. Kawano, (2012) https://www.nndc.bnl.gov/exfor/servlet/E4sMakeE4 (visited on 06/26/2021).

[50] P. N. Brandhoff and K. H. Cats, *Monitoring van reguliere lozingen van radioactiviteit bij niet-nucleaire installaties*, tech. rep. 2019-0176 (Rijksinstituut voor Volksgezondheid en Milieu, 2019).

[51] *Personal communication with Marc-Jan van Goethem.*

Appendices

A Overview data samples

A.1 Comparison of irradiated $NaHCO_3$ and NaCl samples

Table A.1: Mass and calculated number of Na atoms in the $NaHCO_3$ and NaCl samples used in the comparison experiment.

	Mass (g)	Number of Na atoms ($\times 10^{23}$)
$NaHCO_3$	65.7(1)	4.304(8)
NaCl	76.6(2)	7.90(2)

A.2 Thermal neutron absorption

Table A.2: Mass and calculated number of Na atoms in the $NaHCO_3$ and NaCl layers used in the thermal neutron absorption experiment.

	Layer	Mass (g)	Number of Na atoms ($\times 10^{23}$)
$NaHCO_3$ in $NaHCO_3$	Inner $NaHCO_3$	75.6(2)	4.95(1)
	Outer $NaHCO_3$	60.2(2)	3.94(1)
$NaHCO_3$ in NaCl	Inner $NaHCO_3$	73.6(2)	4.82(1)
	Outer NaCl	73.7(2)	7.59(2)

A.3 Neutron flux distribution

Table A.3: Mass and calculated number of Na atoms in the $NaHCO_3$ samples used in the neutron flux distribution experiment.

	Mass (g)	Number of Na atoms ($\times 10^{23}$)
Sample 2	63.0(2)	4.127(8)
Sample 3	64.5(2)	4.226(8)
Sample 4	64.4(2)	4.219(8)
Sample 5	64.5(2)	4.226(8)
Sample 6	64.6(2)	4.232(8)
Sample 7	64.8(2)	4.245(8)
Sample 8	65.4(2)	4.284(8)

A.4 $NaHCO_3$ irradiation at GPTC

Table A.4: Mass and calculated number of Na atoms in the $NaHCO_3$ samples used in the experiment at the GPTC.

	Mass (g)	Number of Na atoms ($\times 10^{23}$)
Sample 1	65.2(2)	4.271(8)
Sample 2	65.4(2)	4.284(8)
Sample 3	65.0(2)	4.258(8)
Sample 4	65.3(2)	4.278(8)
Sample 5	63.9(2)	4.186(8)
Sample 6	65.1(2)	4.265(8)
Sample 7	65.3(2)	4.278(8)
Sample 8	65.1(2)	4.265(8)

Table A.5: Irradiation scheme showing the time after the first irradiation and the relative neutron flux corresponding to each of the 33 irradiations. This scheme was retrieved from Marc-Jan van Goethem.

Time after first irradiation (minutes)	Relative neutron flux	Time after first irradiation (minutes)	Relative neutron flux
0	0.004994501	450	0.035243401
25	0.005932887	480	0.024694613
65	0.045427595	510	0.003071265
90	0.008802958	540	0.013732099
115	0.021784748	569	0.095530448
140	0.025014745	607	0.067169881
170	0.003334706	634	0.004482068
200	0.023002805	657	0.069348556
220	0.024241093	702	0.008740933
240	0.010644161	721	0.030823804
270	0.026719892	745	0.02525929
300	0.00499628	767	0.0478686
320	0.067856831	782	0.040425535
360	0.007368812	809	0.107166351
390	0.020378391	852	0.072841105
415	0.021402146	896	0.019295056
435	0.012404441		

B Analysis pulse-height spectrum of Argon pressure can

In this section, the origin of the identified peaks in the pulse-height spectrum obtained from the irradiated argon pressure can is discussed. For clarity, the pulse-height spectrum is shown again in Figure B.1.

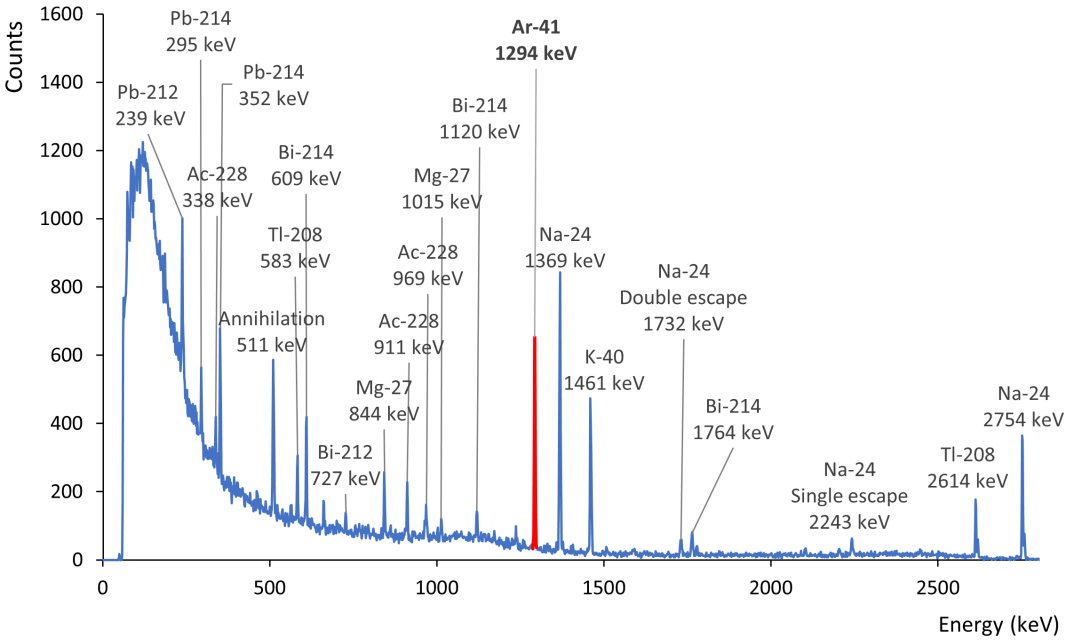

Figure B.1: Obtained pulse-height spectrum for the 1 l argon container. The energy peak corresponding to the decay of ^{41}Ar is marked in red. The peaks visible in the spectrum are indicated by the corresponding gamma-ray energy and radioactive isotope. The peaks were identified with the use of the Lund/LBNL Nuclear Data Search[32].

As stated in Methods subsection 3.4, the argon container is made of aluminium. Aluminium can undergo several types of neutron activation reactions when placed inside an Am-Be source, namely ^{27}Al(n,α)^{24}Na, ^{27}Al(n,p)^{27}Mg and ^{27}Al(n,γ). These lead to the production of ^{24}Na, ^{27}Mg and ^{28}Al, which decay along with the emission of gamma rays. Energy peaks corresponding to the decay of the radionuclides ^{24}Na and ^{27}Mg are visible in the pulse-height spectrum. However, the gamma ray with an energy of 1779 keV, which has a branching ratio of 100%, corresponding to the decay of ^{28}Al is not detected. This is due to the very short half-life of 2.2 minutes corresponding to this decay. When comparing the terms, depending on the decay constant λ and the various time intervals, in Equation 17 for ^{28}Al and ^{41}Ar, it can be calculated that the number of detected photons for ^{28}Al is expected to be less than 0.7% of the number of gamma rays detected for the decay of ^{41}Ar. Since the number of counts in the ^{41}Ar peak was found to be 1320, as mentioned in Results subsection 4.4, less than 10 counts are expected to be detected in the peak of ^{28}Al. Therefore, the peak corresponding to the gamma ray emitted during the decay of ^{28}Al can not be distinguished from the

background in the obtained pulse-height spectrum.

The presence of ^{27}Mg results in the detection of energy peaks at 844 and 1015 keV. The spectrum shows a higher intensity for the 844 keV peak compared to the intensity of the 1015 keV peak. This can be explained by the branching fractions of the two gamma rays. The branching ratio of the 844 keV peak is 71% with respect to 29% for the 1015 keV peak. Moreover, the detection efficiency is larger for the lower energy gamma ray. Therefore, the intensity of the 844 keV is expected to be higher as was obtained in the experiment. Besides ^{27}Mg, ^{24}Na was also produced in the aluminium container. Peaks at 1369 and 2754 keV corresponding to the decay of ^{24}Na are visible in the measured pulse-height spectrum. Moreover, just as for the NaCl and $NaHCO_3$ samples, escape peaks are detected corresponding to the 2754 keV gamma ray of ^{24}Na at energies of 1732 and 2243 keV.

Due to the low activity of argon and the fact that the detector lid was not closed during the measurement, a lot of background peaks are also visible in the spectrum. As mentioned in the theory, the major sources of natural radioactivity are ^{40}K and the daughter atoms of ^{232}Th and ^{238}U. When comparing the peaks in the obtained spectrum with the most intense gamma rays emitted by these naturally occurring radioactive isotopes, as listed in Table 1, similarities can be found.

Firstly, the peak corresponding to the decay of ^{40}K can be observed in the spectrum at 1461 keV. Moreover, the peaks corresponding to ^{212}Pb, ^{228}Ac, ^{208}Tl and ^{212}Bi from the decay chain of ^{232}Th appear in the spectrum. Finally, the remaining gamma-ray peaks observed in the spectrum correspond to the radioactive isotopes ^{214}Pb and ^{214}Bi, which are both descendants of ^{238}U.